Draft version June 3, 2022
Typeset using LaTeX preprint2 style in AASTeX631

The Strength and Variability of the Helium 10830 Å Triplet in Young Stars, and Implications for Exosphere Detection

Daniel M. Krolikowski,[1] Adam L. Kraus,[1] Benjamin M. Tofflemire,[1] and Caroline Morley[1]

[1]*Department of Astronomy, University of Texas at Austin, 2515 Speedway, Stop C1400, Austin, TX 78751, USA*

ABSTRACT

Young exoplanets trace planetary evolution, particularly the atmospheric mass loss that is most dynamic in youth. However, the high activity level of young stars can mask or mimic the spectroscopic signals of atmospheric mass loss. The He 10830 Å triplet is increasingly important in the search for exospheres, but has a complex relationship with stellar activity that is not well understood. To characterize the He-10830 triplet at young ages, we present time-series NIR spectra for young transiting planet hosts taken with the Habitable-zone Planet Finder. The He-10830 absorption strength is similar across our sample, except at the fastest and slowest rotational periods, indicating that young chromospheres are dense and populate metastable helium via collisions. Photoionization and recombination by coronal radiation only affects the helium population at the active and inactive extremes in our sample. Volatility in the stellar activity, such as from flares or changing surface active features, drives variability in the He-10830 triplet. Variability is largest at the youngest ages before decreasing to $5-10$ mÅ (or $1-3\%$) at ages above 300 Myr, and is smallest on the shortest timescales. Intrinsic stellar variability of the He-10830 triplet should not preclude detection of young exospheres, except at the youngest ages, especially if out-of-transit comparison observations are taken directly surrounding transit. Regardless, caution is necessary when interpreting transit observations in the context of stellar activity, as there are many scenarios which can lead to enhanced stellar variability even on timescales of an hour.

Keywords: stellar activity (1580), atomic spectroscopy (2099), stellar chromospheres (230), exoplanet atmospheres (487)

1. INTRODUCTION

Planetary evolution within the first billion years, when stellar activity and planetary orbits are most dynamic, establishes a planet's ultimate atmospheric properties and habitability potential. A planet's birth location in the disk determines the initial mass and composition of atmosphere that can be accreted (Öberg et al. 2011; Ikoma & Hori 2012), and its final orbital configuration after any migration sets the planet's radiative environment and atmospheric retention (Owen & Wu 2013; Shields et al. 2016). A majority of super-Earth to

Corresponding author: Daniel M. Krolikowski
krolikowski@utexas.edu

sub-Neptune sized planets form with a massive H/He envelope that precludes habitability (Wolfgang & Lopez 2015; Owen & Mohanty 2016). Losing this massive, gaseous envelope is necessary to produce habitable conditions, such as favorable surface environment and the creation of a secondary atmosphere (Pierrehumbert & Gaidos 2011; Lammer et al. 2014).

High-energy irradiation can sculpt a massive H/He envelope (Lammer et al. 2003; Kubyshkina et al. 2018), leading to photoevaporative mass loss that will alter the atmosphere's size and composition. This mass loss carves the gap in planet occurrence at a radius of $\sim 1.7 R_{\oplus}$, separating smaller rocky super-Earths from larger sub-Neptunes with gaseous envelopes (Fulton et al. 2017). Photoevaporation is the leading theory for the cause of this atmospheric evolution (Owen & Wu 2013; Lopez & Fortney 2013; Jin et al. 2014), but mass loss could also be driven by heat from the contracting core or impacts (Liu et al. 2015; Ginzburg et al. 2018). The exact mechanism sculpting the atmosphere, and timescale over which it acts, are crucial inputs for models predicting the habitability of exoplanets (Johnstone et al. 2015; Owen & Mohanty 2016).

One way to distinguish different atmospheric evolutionary pathways is to directly detect ongoing mass loss, and correlate the mass-loss rate with system characteristics, such as the host star's spectrum and planet's orbit. Exoplanet transit spectroscopy can detect excess absorption from gas in the evaporating atmosphere, also known as an exosphere. The first exosphere detections were of escaping hydrogen gas using the Lyman-α spectral line (e.g. Vidal-Madjar et al. 2003; Lecavelier Des Etangs et al. 2010; Ehrenreich et al. 2012; Bourrier et al. 2018). Unfortunately, there are difficulties in observing Lyman-α exospheres because the line is heavily absorbed by the interstellar medium, is contaminated by geocoronal emission, and requires expensive space-based observations (Neff et al. 1986; Dring et al. 1997; Ehrenreich et al. 2011). Therefore, Lyman-α exospheres are only detectable around the very nearest planets.

Thankfully, there is an increasingly popular probe of atmospheric mass loss that is free of Lyman-α's complications: the helium 10830 Å triplet feature (Seager & Sasselov 2000; Oklopčić & Hirata 2018), which has been used to detect many exospheres over the last four years (e.g. Spake et al. 2018; Allart et al. 2018; Salz et al. 2018; Ninan et al. 2020; Czesla et al. 2022; Orell-Miquel et al. 2022). This feature is formed from the transition between the two lowest energy He I triplet states (2^3S to 2^3P). Importantly, the 2^3S state is radiatively decoupled from the ground state and thus metastable; a He atom will remain in this state long enough to absorb incoming photons and make the He 10830 Å transition. Ground-based high resolution NIR spectrographs can access this line, enabling survey observations to map atmospheric mass loss across system demographics.

It is crucial to find young exospheres to reveal the mechanisms driving atmospheric mass loss, because the most significant mass loss is expected within the first Gyr when the stellar high-energy radiative output is highest (Micela et al. 1985; Preibisch & Feigelson 2005; Jackson et al. 2012). While a subset of the known young transiting planets have been targeted in the search for helium exospheres (Hirano et al. 2020; Gaidos et al. 2020a,b, 2021; Vissapragada et al. 2021; Gaidos et al. 2022), only one robust detection has been made (HD 73583 b; Zhang et al. 2022). This is not surprising, as young stars have high levels of magnetic activity that introduce chromatic, temporally coherent noise across the stellar spectrum (Desort et al. 2007; Reiners 2012) that can mask or mimic a planetary signal in transmission spectra (Rackham et al. 2018; Boldt et al. 2020).

The stellar He-10830 triplet is chromospheric, and thus is sensitive to stellar activity. This can lead to confusion between a stellar or planetary nature for changes in the He-10830 triplet absorption. The stellar He-10830 triplet of FGKM dwarfs is intrinsically variable (Zirin 1975, 1976; Sanz-Forcada & Dupree 2008; Fuhrmeister et al. 2020), but the connection between this variability and activity is unexplored, particularly at young ages. This complicates the interpretation of changes in the He-10830 triplet absorption strength for transit spectra of young planets.

In the stellar chromosphere, there are two main pathways to populate the metastable state: photoionization and recombination (PR), and collisional excitation (CE). In the PR mechanism, a He atom is photoionized (by photons with $\lambda \leq 504$ Å) and then recombines to populate the metastable state. This process is driven by high energy coronal radiation incident upon He atoms in the upper chromosphere (Goldberg 1939; Zirin 1975). The metastable state can be directly populated through CE from the ground state (Hartmann et al. 1979; Wolff & Heasley 1984), although this requires a dense enough chromosphere for collisions to dominate over the PR mechanism (Sanz-Forcada & Dupree 2008). In exospheres, the PR mechanism driven by high energy instellation would form the feature because the exosphere density is too low for CE. An exosphere's He-10830 triplet signal is thus dependent on its host star's high energy output, particularly the intensity and shape of the stellar UV spectrum (Oklopčić & Hirata 2018; Oklopčić 2019; Poppenhaeger 2022).

Once He atoms populate the metastable state, they can absorb photospheric NIR continuum to excite into the 2^3P state and produce the He-10830 triplet absorption feature. Due to splitting of the 2^3P state, the feature consists of three lines: two blended lines (rest vacuum wavelengths of 10833.217 Å and 10833.306 Å), and a weaker resolved component with a rest vacuum wavelength of 10832.057 Å (Martin 1960). The feature forms higher in the chromosphere than other traditional spectral chromospheric activity indicators (e.g. Ca II H and K, H-α; Dupree et al. 1992; Avrett 1998), and its formation depends on the structure of the chromosphere, transition region, and corona (Avrett et al. 1994; Andretta & Jones 1997).

He-10830 triplet absorption on the Sun is stronger in active regions with higher X-ray emission (Andretta & Jones 1997; Mauas et al. 2005; Andretta et al. 2017) and He-10830 triplet equivalent width correlates with X-ray luminosity for inactive FGK dwarfs (Zarro & Zirin 1986), both implying that the PR mechanism is dominant for inactive solar-type stars. This relation does not hold for active FGK dwarfs because their chromospheres are dense enough for CE to dominate (Sanz-Forcada & Dupree 2008). There is no detectable absorption for SpT $\geq$ M5, due to emission fill-in and reduced line excitation from the PR mechanism (Fuhrmeister et al. 2019).

Volatility of the stellar activity level, from secular changes in the magnetic field and short-term evolution of active events (e.g. surface features, winds, mass loss, or flaring), can cause variability in the He-10830 triplet. This has been observed in FGK dwarfs and giants (although with sparse, telluric-contaminated observations; Zirin 1976; Obrien & Lambert 1986; Katsova & Shcherbakov 1998), and more recently in M-dwarfs (with CARMENES; Fuhrmeister et al. 2020). However, the amplitude and timescale of variability remains uncharacterized for young stars with high activity levels.

To better understand the He-10830 triplet in young stars, and the potential for a stellar signal to mask or mimic an exosphere, its absorption strength and variability must be characterized spanning a range of stellar parameters. We have gathered a data set that is well suited for this task: time series NIR spectroscopy of young transiting planet hosts from the Habitable-zone Planet Finder. With these data, we study the He-10830 triplet across age, spectral type, and activity level to explore the effect of stellar activity on the He-10830 triplet and assess the feasibility of detecting young helium exospheres.

2. DESCRIPTION OF STELLAR SAMPLE AND HPF OBSERVATIONS

We present observations of 10 young transiting planet hosts, comprising all such known systems as of July 2020 that are observable with the HET at McDonald Observatory ($-10° < \delta < 72°$). We obtained these observations for a survey to search for outer giant planets in these systems, which will be described in a forthcoming paper. These 10 stars are a subset of a larger 16 target sample used in the RV planet search survey. The 6 stars that are excluded are faint enough that it is difficult to measure precise and reliable spectral line equivalent widths. This removes all M-dwarfs from our sample, so our study here concerns only FGK dwarfs. The stars in this paper's sample span: ~ 25 Myr to 1 Gyr in age, late-F to late-K in spectral type, and 1.88 days to 37 days in rotation period. Information for the full sample is listed in Table 1, including the targets that are excluded in this analysis.

We obtained NIR spectra with the Habitable-zone Planet Finder (HPF; Mahadevan et al. 2012, 2014) on the 10-m Hobby-Eberly Telescope at McDonald Observatory. HPF is a high-resolution ($R \sim 55000$), fiber-fed, stabilized NIR spectrograph covering z, Y, J bands from 8100 – 12700 Å (Hearty et al. 2014; Stefansson et al. 2016). HPF has a laser frequency comb (LFC) to achieve extremely high quality wavelength calibration, exhibiting ~ 20 cm s^{-1} calibration precision and ~ 1.5 m s^{-1} on sky precision for Barnard's Star (Metcalf et al. 2019). HPF has three fibers: a science, sky, and calibration fiber. The sky fiber provides simultaneous observations of nearby sky to subtract sky background (e.g. Moon contamination or airglow), and the calibration fiber can observe the LFC to provide an instantaneous wavelength solution.

Our observational set up is designed for a precision RV planet search. For targets brighter than $J = 10$ we use an exposure time of 5 minutes, which is the maximum allowed exposure time while simultaneously observing the LFC to avoid LFC saturation. This strategy optimizes target S/N with a precise, instantaneous wavelength calibration. The sole exception is for HD 63433, which is bright enough to reach high S/N in only 3 minutes. The 5 minute exposure scheme was used for targets fainter than $J = 10$ in the first year of observations. From August 2019 onward, we use an exposure time of 10 minutes to reach higher S/N for these fainter objects. We bracket these 10 minute exposures with LFC-only observations to improve the wavelength calibration. This method can correct for HPF drift and provides similarly precise wavelength calibration as LFC-simultaneous observations (Stefansson et al. 2020).

These observations are made using HET's flexible queue-mode scheduling (Shetrone et al. 2007), which allows for observations to be spread throughout the trimester to cover baselines of days to months. Each observation (which we call a "visit") is composed of three sequential exposures to increase signal and average over high-frequency, oscillation-driven stellar RV variation. The sole planned exception to this is an observation of V1298 Tau for Planet b's transit on UT 2019/10/24, during which we obtained 11 sequential exposures. From updated TESS ephemerides (Feinstein et al. 2022), this visit did not occur during transit. There are sometimes unplanned exceptions to this, such

Table 1. HPF young transiting planet host star sample

Object	RA	Dec	J	Membership	Age[a]	$T_{\rm eff}$	$P_{\rm rot}$	$N_{\rm ep}$[b]	Plot Color[c]	Ref[d]
	h m s	d m s	mag		Myr	K	d			
Objects included in helium analysis										
V1298 Tau	04 05 19.6	+20 09 25.6	8.7	Taurus	28	4970	2.851	42		11,12
K2-284	05 16 33.8	+20 15 18.4	10.9	Field	120	4140	8.88	13		10
TOI 2048	15 51 41.8	+52 18 22.7	9.9	Group X	300	5185	7.97	13		14
HD 63433	07 49 55.1	+27 21 47.5	5.6	Ursa Major	414	5640	6.45	13		13
HD 283869	04 47 41.8	+26 09 00.8	8.4	Hyades	700	4655	37	15		8
K2-136	04 29 38.9	+22 52 57.8	9.1	Hyades	700	4499	15	36		5,6,7
K2-100	08 38 24.30	+20 06 21.83	9.5	Praesepe	700	6120	4.3	29		4
K2-101	08 41 22.58	+18 56 01.95	11.2	Praesepe	700	4819	10.6	3		4
K2-102	08 40 13.45	+19 46 43.71	11.3	Praesepe	700	4695	11.5	5		4
K2-77	03 40 54.8	+12 34 21.4	10.4	Field	850	4970	19.8	13		3
Objects not included in helium analysis										
K2-25	04 13 05.6	+15 14 52.0	11.3	Hyades	700	3207	1.88	31	–	1,2
K2-103	08 41 38.49	+17 38 24.08	12.3	Praesepe	700	3880	14.6	4	–	4
K2-104	08 38 32.84	+19 46 25.59	12.9	Praesepe	700	3660	9.3	4	–	4
K2-264	08 45 26.05	+19 41 54.46	13.1	Praesepe	700	3580	22.8	6	–	9
EPIC 211901114	08 41 35.69	+18 44 34.98	13.2	Praesepe	700	3440	8.6	3	–	4
K2-95	08 37 27.06	+18 58 36.02	13.3	Praesepe	700	3410	23.9	4	–	4

[a]We adopt the same age for Hyades and Praesepe, 700 Myr, which is roughly the average of previous age determinations (Brandt & Huang 2015; Martín et al. 2018; Gossage et al. 2018). The age for V1298 Tau comes from Johnson et al. (2022), and all other ages are from the planet discovery papers.

[b]Number of in-hand and usable visits for each target through 10/18/2021.

[c]Color used for each object's plotted point in Figures 6, 7, 8, 9, 11

[d]Planet discovery references: (1) Mann et al. (2016), (2) David et al. (2016), (3) Gaidos et al. (2017), (4) Mann et al. (2017), (5) Mann et al. (2018), (6) Ciardi et al. (2018), (7) Livingston et al. (2018), (8) Vanderburg et al. (2018), (9) Rizzuto et al. (2018), (10) David et al. (2018), (11) David et al. (2019b), (12) David et al. (2019a), (13) Mann et al. (2020), (14) Newton, et al. submitted

as when additional exposures are taken due to poor S/N from passing clouds.

The raw 2D images were reduced to 1D spectra using the HPF team's custom pipeline following the procedures of Ninan et al. (2018), Kaplan et al. (2019) and Metcalf et al. (2019). We correct the derived wavelength solution for barycentric motion using barycentric velocities calculated at each exposure time using `barycorrpy` (Kanodia & Wright 2018), which is a Python implementation of the formalism from Wright & Eastman (2014).

We began observations in November of 2018, and the program is still ongoing. All targets have time series spanning at least 9 months, with roughly half of the targets having observations spanning the entire two and a half year program. This unique data set – namely time series, high resolution NIR spectra of young planet hosts – enables us to study the strength and intrinsic variability of the stellar He-10830 triplet at young ages.

3. MEASURING SPECTRAL LINE EQUIVALENT WIDTHS

To study the behavior of the He-10830 triplet at young ages, we measure the feature's equivalent width (EW) from the HPF spectral time series for each star. For this analysis, we must first correct the spectra for telluric contamination before measuring the EWs. We describe our procedures for both of these steps in this section.

3.1. *Correcting telluric contamination*

The region of interest around the He-10830 triplet contains significant telluric contamination, including sky emission and water absorption. These telluric features can significantly affect the measurement precision of the He-10830 triplet's EW and line profile shape, the latter of which is needed to detect velocity structure and study planetary outflow dynamics. There are drawbacks to both empirical and theoretical telluric modeling, and adequately removing the contamination is a difficult task.

One way to avoid telluric contamination is to observe targets when the strong features do not directly overlap the He-10830 triplet, due to the Doppler shift of the stellar spectral lines from relative motion between the target and the Earth. However, this strategy cannot be used for all targets because it is possible that the barycentric motion of a given object during its peak observability places the telluric features within the He-10830 triplet region. This can be an even more pressing issue for the time-sensitive constraints of transit observations.

This is particularly a problem for the nearby young clusters and associations hosting a majority of the known young transiting planets. We calculated the wavelength of the strong sky emission line near the He-10830 triplet in the rest-frame of a variety of these young stellar associations (Hyades, Praesepe, Pleiades, Taurus, Ursa Major, and Group X) across the year for observations taken at McDonald Observatory. On average, the emission line is 1 Å from the strong, red component of the He-10830 triplet, ranging from 2.7 Å to directly overlapping the He line. The young clusters along the ecliptic that were accessible by K2 feature the worst contamination. This highlights the importance of TESS's all-sky search which includes many other young stellar associations (including Ursa Major and Group X). It is therefore crucial to adequately correct for this telluric contamination. Below, we describe our methods for removing sky emission lines (Section 3.1.1) and water absorption features (Section 3.1.2).

3.1.1. *Subtraction of sky emission lines*

There are three sky emission lines in the He-10830 triplet spectral region: one strong line (which is actually an unresolved doublet) with a rest vacuum wavelength of 10834.2895 Å, and a weaker resolved doublet at 10832.103 Å and 10832.412 Å (Oliva et al. 2015). In principle, the presence of sky emission lines should not be an issue because HPF has a dedicated fiber to simultaneously observe blank sky during every visit. The spectrum observed by this fiber, $f_{\rm sky}$, could then be subtracted from the science fiber spectrum, $f_{\rm sci}$, to produce a telluric emission free spectrum, $f_{\rm skysub}$. However, this naive sky subtraction often results in an over-subtraction of the emission lines in HPF data, introducing residual absorption artifacts in the resultant spectrum. Figure 1 shows the result of a naive sky subtraction with HPF data of the A-star HR 5162. It is difficult to assess the amount of over-subtraction in stars of later type due to the multiple stellar lines near the He-10830 triplet, but the lack of stellar features in the A-star spectrum highlights the over-subtraction.

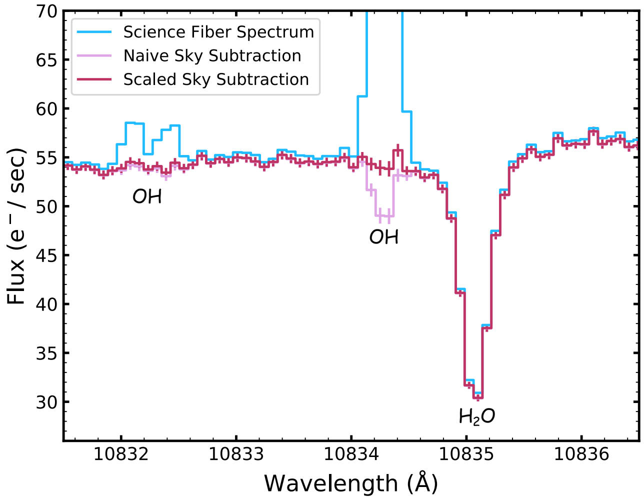

Figure 1. The spectral region around the He-10830 triplet for the A2 star HR 5162. We show an A-star to highlight the emission line over-subtraction as it is devoid of stellar absorption lines. The cyan spectrum is the science fiber flux prior to sky subtraction, which shows the sky emission lines, and the pink spectrum is the sky-subtracted spectrum following naive subtraction. For the strongest sky line, the over-subtraction is roughly 10% of the nearby continuum, which is significantly larger than the measurement error. The red spectrum shows the sky-subtracted spectrum using the scale factor β determined from the sky emission line at 10289.5 Å. The scaling removes the over-subtraction, and the resultant spectrum agrees with the nearby continuum within errors. Both subtraction methods are adequate and agree for the nearby weak emission doublet.

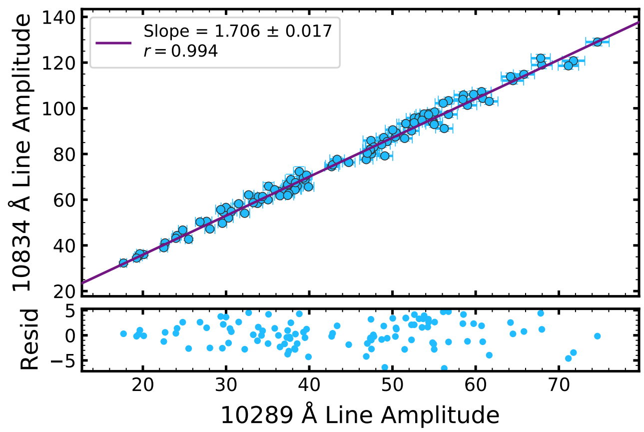

Figure 2. Comparison of the amplitudes for the strong sky emission line near the He-10830 triplet (λ = 10834.3 Å) and the calibration sky emission line (λ = 10289.5 Å) used to determine the sky subtraction scale factor β. The amplitudes of the emission lines are well-correlated, and their relationship is linear over an order of magnitude in amplitude.

The degree to which the emission lines are over-subtracted depends on the relative flux from the target and the sky, which is demonstrated by the lack of over-subtraction for the weak emission doublet in Figure 1. The over-subtraction residual approaches the measurement uncertainty, and eventually disappears, as the ratio of the target flux to the peak of the sky emission line increases. This means that the brightest targets will have no significant over-subtraction. Therefore, over-subtraction is a greater issue for bright sky emission lines and "faint" targets. This applies to many of our observations: the emission line at 10834.2895 Å is bright enough, and many of our young transiting planet host sample are faint enough, for the over-subtraction to be significant.

A better method for sky subtraction would involve scaling the sky fiber flux to account for the difference between the science and sky fiber fluxes (such as from throughput differences). Most simply, we can do this by multiplying the entire sky spectrum by a scalar value, which we call β. The equation describing the sky subtraction is then:

$$f_{\text{skysub}} = f_{\text{sci}} - \beta f_{\text{sky}} \tag{1}$$

To determine β for each observation, we could fit the spectrum around the sky emission line and find the β value that results in a spectrum closest to the nearby continuum. However, we cannot use the region around the He-10830 triplet to determine β because there is no clear continuum due to the presence of multiple stellar and telluric absorption features.

We instead use a different strong sky emission line that is isolated from other spectral features to measure β. We assume that the OH sky emission lines all behave similarly because their strength should largely be a product of sky conditions, although there may be slight differences depending on the physics of the transitions. We searched the full HPF spectral range for a sky emission line of similar strength to the line at 10834 Å to use as a calibrator line. While there are many strong sky lines throughout the HPF bandpass, a vast majority of them reside in regions with many stellar and telluric absorption features. We were able to identify one high quality candidate calibration sky emission line without any nearby absorption features: an unresolved doublet with a rest vacuum wavelength of 10289.455 Å. Figure 2 shows a comparison of the two sky emission line amplitudes using the sky fiber spectra from our observations of K2-136. The amplitudes are well-correlated with minimal scatter, and we conclude that this sky emission line is an adequate calibrator with which to determine β.

To calculate β, we find the scale factor needed to match the calibration line flux in the sky fiber spectrum to that of the science fiber spectrum (thus accounting for underlying continuum flux). We perform a minimization to find the best fit β value, represented as:

$$\min_{\beta} \ \mathrm{stdev}\left(\frac{f_{\mathrm{sci}} - \beta f_{\mathrm{sky}}}{f_{\mathrm{cont}}}\right) \tag{2}$$

We perform the minimization over a 2.5 Å region around the calibration line between 10288.105 Å and 10290.605 Å. The sky fiber spectrum is scaled and subtracted from the science fiber spectrum, and then fit with a line to obtain a rough estimate of the continuum in the region, f_{cont}. The best fit β is the scale factor such that the standard deviation of the continuum-normalized, scaled sky subtracted spectrum is minimized. We use the adopted β value to scale the entire sky spectrum and subtract it from the science fiber spectrum to produce the sky-free spectrum as described in Equation 1.

Figure 1 shows the scaled sky subtraction of the A-star HR 5162 in the He-10830 triplet region. The scaling factor works well, and the sky-free spectrum at the location of the strong sky emission line agrees with the nearby continuum value within measurement uncertainty. This demonstrates that the β value determined using the calibrator can be applied to the rest of the sky spectrum, and we perform this corrected sky subtraction method for nearly all data presented in this paper. The only exception is for the target HD 63433, which is bright enough for over-subtraction to not be a significant issue. Thus, we naively subtract the sky emission for all spectra of HD 63433.

3.1.2. *Telluric absorption correction*

There are also two water absorption features in the He-10830 triplet region that can affect EW measurement: a strong line with a rest vacuum wavelength of 10835.08 Å that can often overlap the He-10830 triplet and a weaker line with a rest vacuum wavelength of 10836.95 Å. Telluric standard observations are not taken regularly with HPF as the overhead for these observations is impractical for typical programs. Without observed standards, we can not empirically correct for telluric absorption features in our data. Masking the spectra near strong telluric absorption features would exclude important spectral information, especially because the strong water line often directly overlaps the He-10830 triplet profile.

Given these analysis constraints, we decided to generate theoretical telluric absorption models that are custom fit for each individual observation. We use the `TelFit` python package (Gullikson 2014), which can generate telluric absorption models and iteratively fit data for the best parameter values. We only fit for the humidity value because the humidity provided in the observation header is often not close to

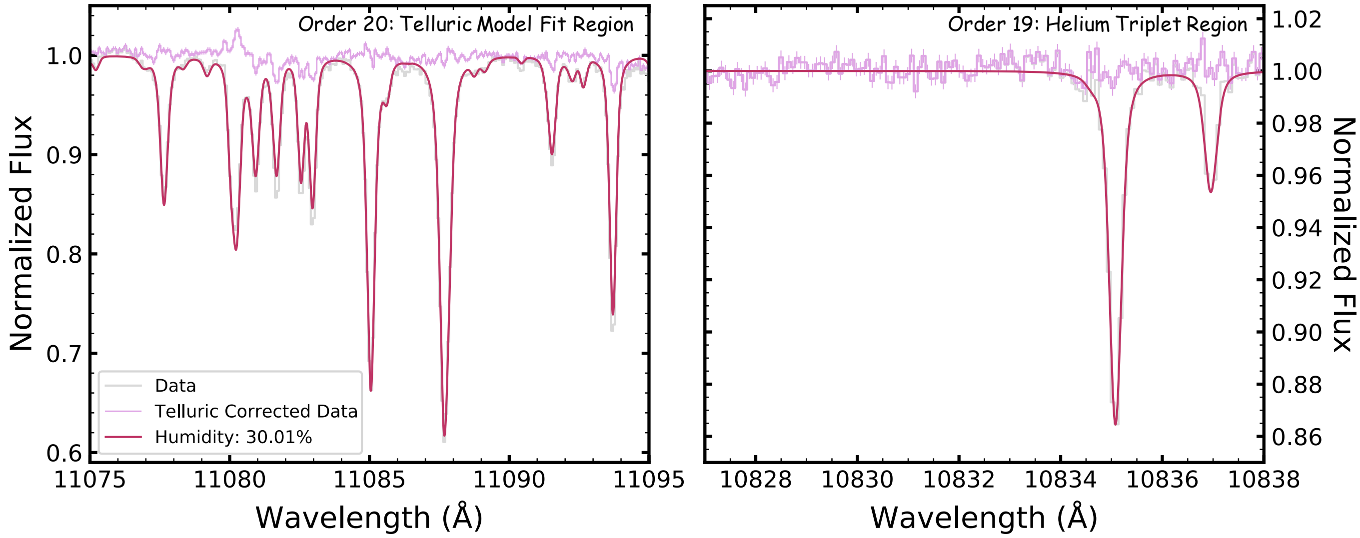

Figure 3. Telluric absorption model fitting for the A-star HR 3711. The gray spectrum shows the sky-subtracted, continuum-normalized data, the red spectrum is the best-fit telluric model, and the pink spectrum is the telluric-corrected spectrum. *Left Panel:* The region in spectral order 20 used to find the best-fit model. There are slight residuals likely due to continuum division or theoretical model imperfections. *Right panel:* The He-10830 triplet spectral region. The two strong water lines are well-corrected. The resulting residuals across the range shown is 0.4%, which is very close to the typical measurement uncertainty of 0.3%.

producing a well-fitting model, and humidity has the largest effect on the telluric model itself. During the fitting process, we fix the spectral resolution to the instrument resolution of 55000.

Using 43 A-star observations from a telluric standard library that has been slowly built since HPF's commissioning, we ran telluric fits on all spectral orders except for those with very strong telluric absorption bands to assess the fit quality across wavelength. We find a wavelength dependence in the best fit humidity value, where the 6 orders blueward of 1 μm produce a consistently lower humidity value than the 5 orders redward of 1 μm. This is perhaps due to systematic differences in the molecular transition database across wavelength, and is unlikely to be due to the varying presence of stellar spectral features which are largely absent in A-star spectra. We find that the spectral order containing the He-10830 triplet provides humidity values with large scatter relative to the mean humidity value across all orders, indicating that it is not reliable for the fitting process. The typical value found in the He-10830 triplet's order is similar to the subsequent redder order, though, so we use that order for all telluric model fits moving forward.

For the final telluric absorption model fitting, we use a 20 Å wide region in spectral order 20 covering $11075 - 11095$ Å. We use this small region because it has many non-saturated water lines that are separated enough to avoid issues from blending, while having little stellar contamination. By operating on a small spectral segment, we also avoid additional error introduced from the continuum and blaze correction on a full spectral order. With the best fit telluric model parameters from order 20, we then generate a telluric model for the entire HPF bandpass. Figure 3 shows an example of the telluric absorption model fit for the A-star HR 3711. Two spectral regions are shown: the region in spectral order 20 where the fit is performed, and the He-10830 triplet region in spectral order 19. The two water lines in the He-10830 triplet region are well-corrected using the model, leaving us confident in our procedure for removing telluric absorption.

3.2. *Measuring the equivalent width of spectral lines in the He-10830 triplet region*

With telluric contamination removed, we can precisely measure the EW of the He-10830 triplet. The spectral region around the He-10830 triplet has other stellar spectral lines which complicates the measurement of the isolated He-10830 triplet EW. The nearby stellar and telluric features also make it more difficult to define the continuum level directly adjacent to the He-10830 triplet. We therefore fit the entire spectral region from 10822 Å to 10845 Å, including all stellar spectral lines, to provide the best leverage for fitting the continuum level and measuring EWs. This also results in EWs for a handful of other presumably inactive lines that provide useful comparison to the active He-10830 triplet.

Table 2. Spectral lines in the fit region

Element	λ^{a} (Å)	Line Profile
Cs II[b]	10824.6926	Gaussian
Si I	10830.054	Lorentzian
He I	10832.057	Gaussian
He I	10833.2615[c]	Gaussian
Ti I	10836.38	Gaussian
Na I	10837.8435[d]	Gaussian
Ca I	10841.95	Gaussian

[a]Vacuum line center wavelength taken from the NIST atomic spectral line database (Kramida et al. 2021).

[b]This line may be blended with a nearby Cr I line.

[c]The average wavelength of the two blended red components of the helium triplet.

[d]The average wavelength of two close Na I transitions.

In addition to the two resolved components of the He-10830 triplet, there are 5 other prominent stellar spectral lines in this wavelength range, although their strength varies across the range of effective temperatures covered in our sample. All of the stellar spectral lines included in fits of this region are listed in Table 2. The nearby strong silicon line is the closest spectral feature to the He-10830 triplet in wavelength, which it overlaps with its broad wings. The other lines do not directly contaminate the He-10830 triplet, and are relatively weak and narrow.

Our spectral model has three components: 1) the combined profiles of the 7 spectral lines listed in Table 2, 2) the telluric model that is separately fit for each individual exposure (as described in Section 3.1.2), and 3) a 2nd order polynomial continuum. We model the silicon line profile with a Lorentzian due to its wide wings, and the other 6 line profiles with Gaussians. In our data processing pipeline, we use an iterative b-spline to fit the continuum level of the entire He-10830 triplet spectral order. For this subset of the spectral order, we initialize the continuum parameters by fitting a polynomial to the b-spline continuum only for the 23 Å region we study here. The full model is described as:

$$f(\lambda)_{\rm model} = C(\lambda)\ f(\lambda)_{\rm tell} \sum_{i=1}^{N_{\rm lines}} p(\lambda, A_i, \mu_i, s_i) \quad (3)$$

$$C(\lambda) = c_0 + c_1\lambda + c_2\lambda^2 \quad (4)$$

where $C(\lambda)$ is the continuum polynomial, $f(\lambda)_{\rm tell}$ is the telluric absorption model described in Section 3.1.2, and the summation represents the combined spectral line profiles. In the summation, $N_{\rm lines}$ is the number of spectral lines included in the fit, p is the profile used to describe each particular spectral line listed in Table 2, A is the amplitude of the line profile, μ is the wavelength of the spectral line, and s is the scale factor of the line profile. The scale factor is given by the standard deviation of a Gaussian profile and the scale parameter of a Lorentzian profile. In all, the free parameters in our model are the three continuum polynomial coefficients (c_0, c_1, c_2) and the three parameters describing each spectral line included in the model (A_i, μ_i, s_i). We explicitly remind readers that the telluric absorption model is fit independently prior to the procedure described here.

We modify the model described in Equation 3 for two stars in our sample: K2-100 and V1298 Tau. Both of these stars are rapid rotators, and a stellar rotational broadening profile is not a Gaussian or a Lorentzian. Thus, we rotationally broaden the model using literature measurements of their $v \sin i$. For K2-100, we exclude the Cs and Ti spectral lines because they are too weak at the star's effective temperature to be detectable given the rotational broadening. For V1298 Tau, we exclude the Ti line and the blue component of the He-10830 triplet, which are completely blended with nearby lines. We also modify the continuum for V1298 Tau to be a line, because it is so rapidly rotating that a 2nd order polynomial overfits the blended helium and silicon absorption.

We fit the observed flux after scaled sky subtraction, $f_{\rm skysub}$ (Equation 1), with the model described in Equation 3 using the least squares optimization implemented in `curve_fit` from the `scipy` package (Virtanen et al. 2020). We use the implementation of the Gaussian and Lorentzian profiles from `astropy` (Astropy Collaboration et al. 2013, 2018). We include uncertainties on the observed flux which are calculated by adding in quadrature the errors on the science and sky fiber spectra. Figure 4 shows an example fit of an observation of K2-136. The resultant model captures the continuum level and shape, and adequately fits the individual spectral line profiles.

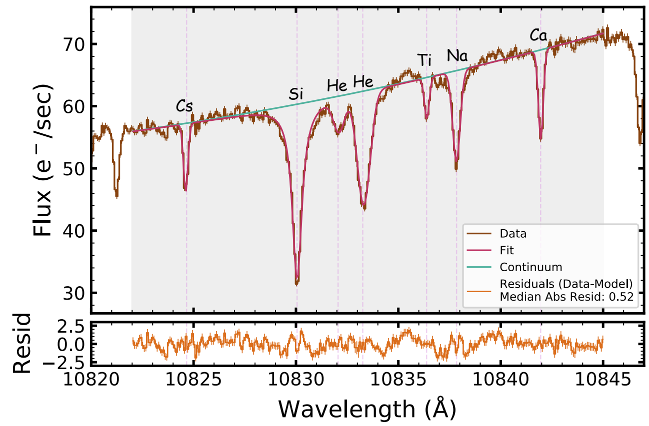

Figure 4. An example result for the spectral fitting of the He-10830 triplet region on an observation of K2-136. The brown spectrum is the telluric-corrected data, the red line is the best fit spectral model, and the teal line is the continuum polynomial. The telluric absorption model has been removed from the data and spectral model to highlight the stellar lines. The bottom panel shows the residuals from subtracting the model from the data. The median absolute residual is 0.52 e$^-$/s, which is comparable to the typical measurement error of 0.5 e$^-$/s. The continuum level and stellar line profiles are well-matched by the model.

We compute EWs for all spectral lines included in each particular star's fits by numerically integrating the observed spectra. We first divide the sky-subtracted spectrum by the best fit model, and fit this residual spectrum with a 2nd order polynomial to remove any remaining continuum shape that may bias the numerical EWs. To assess the quality of the spectral fit and secondary continuum correction, we measure the EW of both the corrected and uncorrected residual spectra, which should be 0. The median residual spectrum EW across all observations is 9.2 ± 17.9 mÅ without the secondary continuum correction, and -0.23 ± 0.76 mÅ following the correction. The EW for the corrected residual spectrum is much closer to 0 and has significantly less variation across observations, showing that our secondary continuum correction is necessary to capture remaining continuum deviations that could affect the numerical EW integration.

For each individual element, we generate a model that includes all spectral lines *except for that element's feature*; for helium this includes the two Gaussian lines for each resolved component of the triplet (except for V1298 Tau which only fits one helium component). We then compute the residual spectrum using this modified model, which will leave only that element's feature in the data, and numerically integrate to compute the EW. We perform sampling, using draws from the spectral model fit parameters and covariance matrix to calculate 1000 residual spectra for each element. We adopt the median and the median absolute deviation (scaled by 1.4826 to be statistically equivalent to the Gaussian standard deviation) of the EW samples as the value and uncertainty.

By direct numerical integration of the data, the EWs will not be affected by potential mismatch between the actual and modeled line profiles. This also accounts for any asymmetries in the spectral lines included in our fit, such as for the inherent asymmetry of the redder component of the He-10830 triplet. As a comparison check, we also computed the EWs analytically from the fit parameters for each spectral line profile. The numerical and analytical values agree within uncertainties. Given the advantages that the numerical EW calculation has with using the data's line profile, we are confident in adopting the numerical EWs for this paper.

Figure 5 shows the EW measurement uncertainty of each spectral line as a function of the median signal-to-noise in the He-10830 triplet spectral order for all targets. The uncertainty

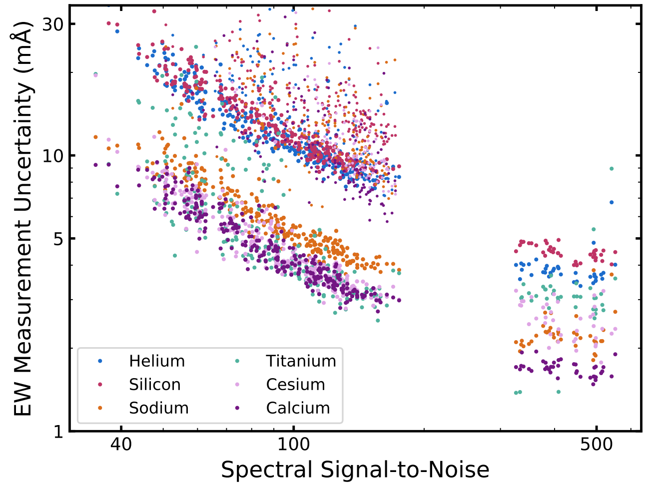

Figure 5. The measurement error of each spectral line for all targets as a function of the median spectrum signal-to-noise in the He-10830 triplet order. The smaller points are measurements for K2-100 and V1298 Tau, which feature larger error than the rest due to their rapid rotation. The inverse relationship expected is shown, and the uncertainty plateaus at $\lesssim 5$ mÅ for the He-10830 triplet above S/N ~ 300.

decreases with increasing signal-to-noise, as expected. The typical uncertainties are larger for helium and silicon compared to the other lines, at least partially due to the fact that they have significantly larger EWs. The two features are also broader, and the silicon line in particular features strong absorption wings. Regardless, the EW uncertainty is in general precise enough to adequately measure the variability of our time series data, and it plateaus at ~ 5 mÅ for the highest quality spectra. Given the typical He EW value (~ 325 mÅ), a single-epoch measurement error of 5 mÅ produces a 1.5 % error in the EW value.

For the rest of the paper, we denote the He-10830 triplet EW as EW[He]; for the objects with both resolved components fit, this value is the sum of the individual component EWs. Table 3 shows all EW[He] measurements, and provides an explanation for observations with-

Table 3. Helium 10830 Å Triplet EW Measurements

Date (JD)	EW[He] mÅ	$\sigma_{\mathrm{EW[He]}}$ mÅ	Flag[a]
K2-136			
2458425.972	315.26	10.43	-
2458425.976	307.7	12.42	-
2458425.98	326.86	12.29	-
V1298 Tau			
2458548.609	409.43	10.77	-
2458548.613	-	-	1
2458548.618	456.2	36.62	-

Small sample of EW measurements shown, all measurements are in the machine readable table file.

[a]Flag denoting the reason for missing EW measurement: (1) Low spectrum S/N, (2) failed spectral fit, (3) bad spectral fit.

out a calculated EW[He] (from low spectral S/N or a failed spectral fit).

4. TIME SERIES PROPERTIES OF THE HE TRIPLET

The line profile of the He-10830 triplet probes the conditions in the stellar atmosphere from which the line arises. Different line formation pathways (e.g. the photoionization-recombination mechanism or collisional excitation) will set the dependence of absorption strength on various stellar properties and is indicative of the stellar activity level (Zarro & Zirin 1986; Sanz-Forcada & Dupree 2008). Evolution in the stellar activity can cause variability in the line strength, and the amplitude and timescale of variation can indicate the types of active features that affect the He-10830 triplet (Zirin 1976; Fuhrmeister et al. 2020). With our sample, we have a unique window into the He-10830 triplet in *young* active stars spanning age and spectral type.

4.1. *He-10830 triplet absorption strength*

The top panel of Figure 6 shows the median EW[He] as a function of T_{eff} for each star in our sample, along with literature values of inactive and active dwarfs. Relative to stars of the same effective temperature, the young stars in our sample show EW[He] that is enhanced over inactive dwarf stars (Zarro & Zirin 1986) and comparable to active dwarf stars (Sanz-Forcada & Dupree 2008). The correlation between EW[He] and T_{eff} is consistent with a flat slope. This agrees with previous literature studies, in which no dependence on T_{eff} has been found for either inactive or active dwarf stars within this temperature range. From the lack of temperature dependence in our sample, we conclude that the stellar atmospheric conditions that lead to the formation of the He-10830 triplet are roughly the same for late-F to late-K dwarfs with $\tau \leq 1$ Gyr. Table 4 shows the EW[He] median value and variability metrics for our sample described in the following subsections.

The EW values of the nearby Ca I 10842 Å line are shown in the bottom panel of Figure 6. There is a strong decrease in strength with increasing T_{eff}, and a turnover at cooler temperatures. This highlights the difference in the line formation pathways between the chromospheric He-10830 triplet and the largely photospheric Ca I 10842 Å line. The Ca I 10842 Å EW-T_{eff} trend we find follows predictions from the photospheric PHOENIX spectral models (Husser et al. 2013).

However, there are two outliers in the EW[He]-T_{eff} plane amongst our sample. This is likely explained by the stellar activity level, which can affect the population of metastable helium and therefore the absorption strength.

Table 4. Overview of Helium EW Measurements

Object	med[EW_{He}]	$\sigma_{med[EW_{He}]}$	mad[EW_{He}]	excess mad[EW_{He}][a]	med[$\sigma_{EW_{He}}$][b]
	mÅ	mÅ	mÅ	mÅ	mÅ
V1298 Tau	447.6	5.8	63.7	62.9	9.72
K2-284	315.8	4.7	26.9	22.5	16.14
TOI 2048	316.2	2.1	13.1	2.1	13.30
HD 63433	315.5	1.4	8.8	8.2	3.75
HD 283869	191.3	2.0	11.8	6.8	9.27
K2-136	302.2	1.3	13.2	8.2	10.20
K2-100	349.6	2.4	19.6	0.0	20.71
K2-101	323.1	3.3	8.7	0.0	22.59
K2-102	303.3	4.2	13.9	0.0	20.22
K2-77	309.0	2.6	14.5	0.0	15.49

[a]The intrinsic scatter of the He EW time series after deconvolving the measurement uncertainty.

[b]The median measurement uncertainty on the He EW from an individual exposure.

One of the outliers is V1298 Tau, which is by far the youngest star in our sample ($\tau \sim 25$ Myr). The other is HD 283869, which is a peculiarly inactive Hyades member (Vanderburg et al. 2018). As a proxy for activity level, we plot EW[He] as a function of stellar rotation period in Figure 7. There is a clear variation in the absorption strength with respect to the rotation period: it is very strong at the fastest rotation, decreases through ~ 5 days, plateaus between 5 and ~ 20 days, and then has a significant decrease in strength by ~ 35 days. We note for comparison that the photospheric Ca I 10842 Å line does not show a rotation period dependence after removing the line's $T_{\rm eff}$ dependence.

It is unsurprising that V1298 Tau would have the strongest He-10830 absorption strength in our sample because it is the most active due to its youth and rapid rotation. V1298 Tau is known to flare (David et al. 2019b,a; Vissapragada et al. 2021; Feinstein et al. 2022), has a photometric variability amplitude indicative of a large spot filling fraction (David et al. 2019b), and potential spectroscopic indications of spots surrounded by facular regions (Feinstein et al. 2021). All of these can enhance absorption in the He-10830 triplet, as well as lead to greater variability in its absorption strength (see Section 4.2).

Interestingly, V1298 Tau has higher EW[He] than the maximum predicted by models with spot filling factors of unity from Andretta & Giampapa (1995). One reason this may be the case is that V1298 Tau has a lower $T_{\rm eff}$ than the models, which Andretta & Giampapa (1995) state may be an issue for K-type stars. V1298 Tau's youth may also increase the He-10830 triplet absorption strength further. At such a young age, V1298 Tau has a lower surface gravity than the rest of the sample. This may produce a larger chromospheric scale height which would increase the path length of photospheric continuum through chromospheric metastable helium, increasing the number of He-10830 triplet absorptions. K2-100 has the second highest EW[He] in our sample, which is unsurprising as it is also the second fastest rotator. This enhanced absorption strength is de-

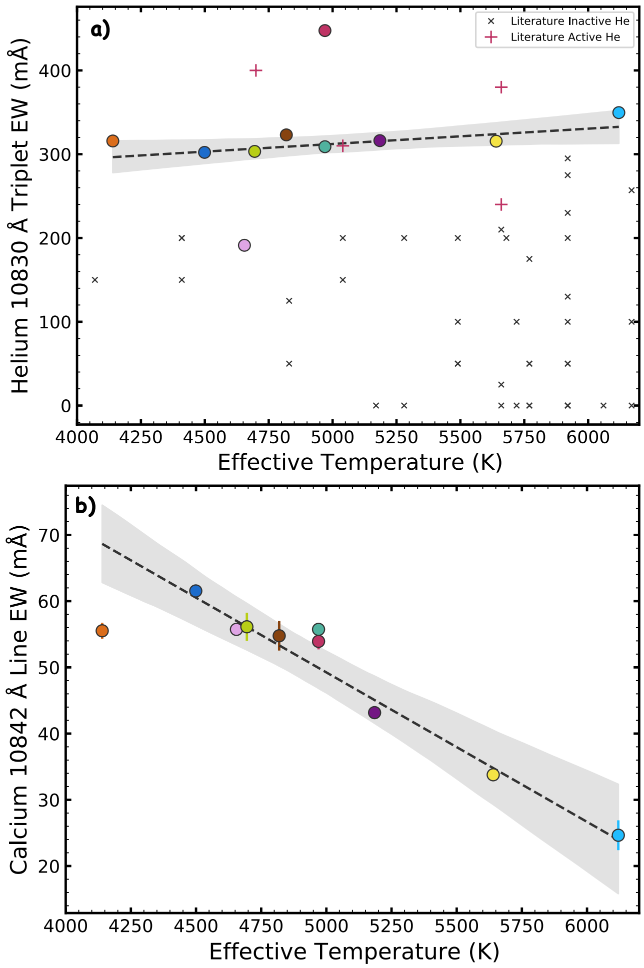

Figure 6. EW[He] (top panel) and the Ca I 10842 Å line (bottom panel) as a function of effective temperature. Our sample is plotted as large colored circles, and values are taken as the median of the time series measurements. The uncertainties are often smaller than the points. In the top panel, the black x's and red +'s show literature He-10830 triplet EWs for field inactive (Zarro & Zirin 1986) and active (Sanz-Forcada & Dupree 2008) dwarfs respectively. Our young stars have EW[He] above the inactive dwarfs, confirming that active stars feature enhanced He-10830 triplet absorption. The dashed line and gray shaded region show a linear fit and 3σ-range for the EW-$T_{\rm eff}$ relation. The EW[He] outliers (V1298 Tau and HD 283869) are excluded from the helium-$T_{\rm eff}$ fit. The chromospheric He-10830 triplet has no $T_{\rm eff}$ dependence, unlike the photospheric Ca I 10842 Å line, highlighting the difference in line formation.

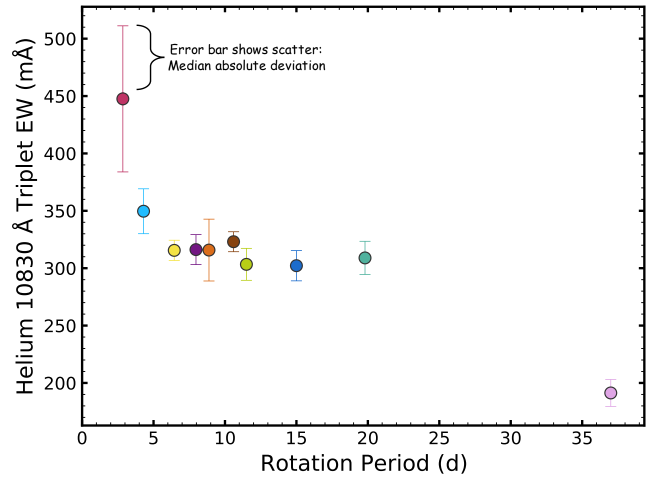

Figure 7. EW[He] as a function of stellar rotation period for our sample. The error bars are the median absolute deviation in EW[He] to show the amplitude of variability as compared to the EW[He] value (note this is not the uncertainty on the median EW[He]). He-10830 triplet absorption shows a clear morphology with the stellar rotation period: more absorption at shorter rotation periods, leading to a plateau below $P_{\rm rot} \sim 20$ d, before decreasing at the longest rotation period. This is indicative of the He-10830 feature's nature as an activity sensitive line: stars with shorter rotation periods have more intense high-energy coronal radiation and denser chromospheres, both of which help to form the stellar He-10830 feature.

spite its older age, and may indicate that the structure of rapidly rotating stars introduces departures from the models of Andretta & Giampapa (1995).

HD 283869 has a long rotation period (nearly double that of the next slowest rotator in our sample), and weaker activity than other Hyades members (from Ca II HK and H-α; Vanderburg et al. 2018). Given the strong dependence of the He-10830 absorption strength on activity, it follows that our data would show weak absorption relative to more rapidly rotating stars. HD 283869 still resides at the upper envelope of the inactive dwarf He-10830 absorption sequence, so it may represent a transition between the active and inactive populations. Unfortunately, we do not observe stars with rotation periods between 20 and 35 days, which would help to clarify the nature of the weakening absorption (e.g. a gradual decline or a sharp discontinuity). Despite its lower EW[He] and slower rotation, HD 283869 is the same mass as fellow Hyades member K2-136. Surface gravity cannot explain the difference in absorption strength for this case.

While our sample does not cover a large range in $T_{\rm eff}$ or age, the stellar high-energy spectral distributions should still be changing across our targets. Differences in high-energy radiative output (such as in X-rays) would change the metastable helium population level if the PR mechanism dominates, in turn changing the He-10830 triplet absorption strength. Not all of our sample stars have literature X-ray observations, but given their rotation periods and masses they almost all likely fall above the saturated x-ray luminosity regime (Pizzolato et al. 2003; Douglas et al. 2014; Núñez et al. 2015). Our results showing a lack of dependence on $T_{\rm eff}$ or rotation period (within 5 to 20 days) reinforces the conclusion from Sanz-Forcada & Dupree (2008) that CE is more important than the PR mechanism in driving the population of metastable helium for active stars. This is likely due to active stars having hotter and denser chromospheres. In the EW[He]-rotation period plateau, CE dominates any decrease in PR excitation from decreasing high-energy coronal radiation, leading to no change in the EW.

At the fastest rotation, V1298 Tau's enhanced He-10830 triplet absorption shows how greater high-energy coronal radiation can compound the effect of CE in the young, high activity regime. At the slowest rotation, HD 283869 represents a bridge between CE and PR dominated metastable helium excitation. The decrease in both the PR mechanism from lower high-energy coronal radiation and CE from the less-active chromosphere conspire to reduce the He-10830 triplet absorption strength.

4.2. *Amplitude of variability in the He-10830 triplet's absorption strength*

Figure 8 shows that the stars in our sample span a wide range of EW[He] variability, which is quantified in the top panel by the median absolute deviation as a function of age. We also compute an "intrinsic" variability quantity, which is plotted in the bottom panel, to show the amount of EW[He] variability that cannot be explained by the measurement uncertainty. The variability in EW[He] is very large at the youngest ages before expeditiously decreasing at older ages. This relation exists in both the full time series and "intrinsic" scatter quantities, indicating that the variability is indeed intrinsic to the stars. Beyond $\tau \sim 300$ Myr the intrinsic variability in EW[He] plateaus at $\sim 5-10$ mÅ. This is contrasted with the Ca I 10842 Å line, which has a slight increase in variability towards youth but with a much smaller variability amplitude across age.

The variability we find at $\tau \gtrsim 300$ Myr is comparable to the field M-dwarfs studied by Fuhrmeister et al. (2020). The median variability across their sample is ~ 12 mÅ (quantified as the median absolute deviation, as we do), which is similar to the plateau in variability at older ages in our sample (see top panel of Figure 8). While the strength of He-10830 absorption greatly decreases through the M-dwarf regime, this result shows that above ages of 300 Myr, the activity-induced variability does not have a significant spectral type dependence through SpT $\sim$ M3. The younger V1298 Tau and K2-284 have larger variability amplitudes than typical for the early M-dwarfs. K2-284 has variability comparable to the late M-dwarfs and V1298 Tau has variability larger than all but a few of the M-dwarfs in the CARMENES sample. Activity-induced variability is most significant at young ages and low effective temperatures.

While variability increases significantly at younger ages, there is no correlation between

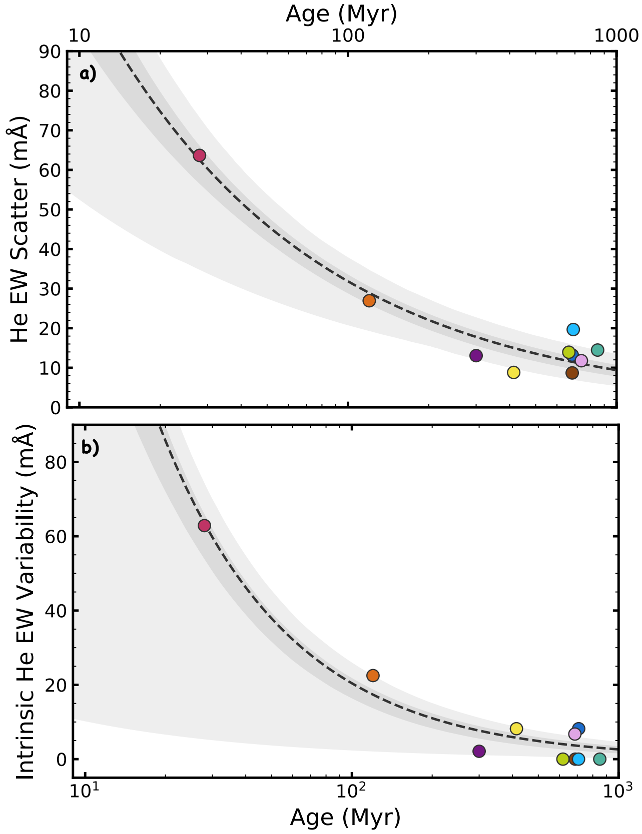

Figure 8. Long-term time-averaged variability of EW[He] as a function of age for our sample. The dashed lines show power law fits to the data, with the shaded regions denoting the 1-σ (darker gray) and 3-σ (lighter gray) intervals. The plotted ages for the Hyades and Praesepe members are artificially spread to avoid overlapping points. *Top panel:* The variability shown is the median absolute deviation of the EW[He] time series, scaled by 1.4826 to be statistically equivalent to the Gaussian standard deviation. Using the MAD accounts for outliers from low spectral S/N or poor spectral fitting. The variability decreases with age, plateauing above 300 Myr at roughly 10 mÅ. The variability increases significantly at younger ages, but the relation is ill-defined due to only having two targets with $\tau \leq 120$ Myr. *Bottom panel:* The variability shown is an "intrinsic" scatter term, quantifying the EW variability that cannot be accounted for with the measurement uncertainty. The variability-age relation persists, showing that the relation is intrinsic to the stars. The objects at the oldest ages are in agreement with intrinsic variability between $5 - 10$ mÅ.

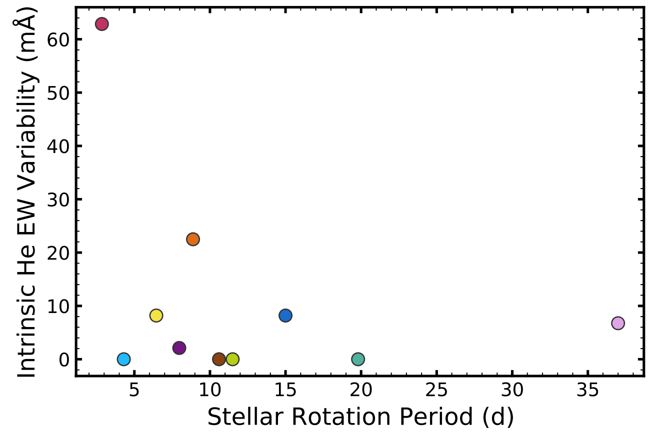

Figure 9. Intrinsic variability of EW[He] as a function of stellar rotation period. There is no relation between the variability and rotation period, which we use as a proxy for activity level. This is unlike for the EW itself, which correlates with the rotation period. The two objects with high variability (V1298 Tau and K2-284) are younger than the rest of the sample.

variability and rotation period. Figure 9 shows the "intrinsic" variability of EW[He] as a function of stellar rotation period. The two outliers with elevated scatter are the young objects in our sample ($\tau \leq 120$ Myr), while the older stars with fast rotation have comparable scatter to the most slowly rotating star. This contrasts with the dependence of EW[He] on rotation period, which we use as a proxy of activity level, shown in Figure 7.

We conclude that the variability in the He-10830 triplet absorption strength is set by activity evolution. Examples of this would be from acute changes in the He-10830 absorption strength (e.g. from flares; Vissapragada et al. 2021), short-term variability from rotational modulation of active regions (e.g. spots and plage, as on the sun; e.g. Brajša et al. 1996), and long term activity cycles (as seen for solar-type stars in other chromospheric lines such as Ca II H and K; e.g. Baliunas et al. 1995; Boro Saikia et al. 2022). We show that the long-term time-averaged variability in EW[He] is stable and relatively low for stars with $\tau \gtrsim 300$ Myr,

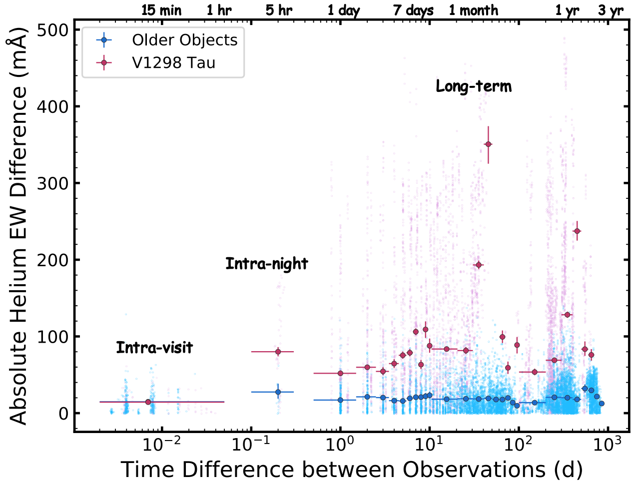

Figure 10. The "EW difference power spectrum" of the He-10830 triplet time series for our targets. We compute the pairwise difference in the EW[He] for each observation of a particular target as a function of the time separating the observations. We stack the "EW difference power spectra" for all targets besides V1298 Tau, as they are older and have lower long-term average variability. The small background points show all pairwise differences, and the large foreground points show the "EW difference power spectra" time baseline-binned to reflect the typical variability at each timescale. The variability is smallest at the shortest timescales, increases after only a few hours, and plateaus out to separations of years.

meaning that even observations separated by months to years should have a comparable He-10830 baseline. Stars older than 300 Myr seem to behave like field stars. This is categorically not true for younger stars, although observations of additional stars with ages between $50 - 300$ Myr are needed to fully map the variability dependence. Such measurements will become available as NIR RV surveys of young stars continue (e.g. Tran et al. 2021).

4.3. *Timescale of variability in the He-10830 triplet*

Our above analysis of the He-10830 triplet absorption variability represents the time-averaged variability over the full observation baseline of our targets, spanning minutes through years. While this provides insight into the typical variability amplitude of the He-10830 triplet, it does not reveal the timescale over which this variability occurs. As exosphere observations are inherently temporal, the timescale of variability is crucial to assess the feasibility of young exosphere detection. Most exosphere detection programs include out-of-transit observations on the same night as the transit, which would be affected by stellar variability on timescales of hours. Our long-term variability analysis shows the limits of comparing observations over full observing seasons (weeks to months to years). We must investigate the timescale of variability in EW[He] to assess out-of-transit observation comparison at shorter time baselines.

To quantify the He-10830 triplet variability as a function of the time baseline between observations we compute an "EW difference power spectrum". For each target, we calculate the difference in the EW[He] for each pair of observations as a function of the time separation of the observations, and we show the result in Figure 10. The "EW difference power spectra" for all targets besides V1298 Tau are stacked to increase precision, because they have roughly the same amount of long-term average variability and because these "older" stars appear to act similarly. V1298 Tau is plotted separately to highlight the increased variability at the youngest ages.

At the shortest timescales ($\Delta t \lesssim 1$ hr), the variability is lower than for longer time baselines, and the same for both the "older" objects and V1298 Tau. Thus, the variability should not be a significant issue for even the youngest stars on timescales of an hour, outside of acute changes in He-10830 triplet absorption (e.g. flaring). For the "older" objects, the variability increases slightly beyond $\Delta t \sim 5$ hr, and is then relatively stable at longer timescales.

The variability for V1298 Tau follows a similar morphology, but has a *much* larger amplitude, even on the same night, which is expected given its larger long-term variability and the increased volatility in activity at young ages.

The typical EW variability increases significantly even after just a few hours, represented by the second binned data point at 5 hours in Figure 10. The only two targets with observations covering this baseline are V1298 Tau and K2-100, both of which have relatively short rotation periods. It is possible that the heightened variability on this timescale is from active regions of varying He-10830 absorption strength beginning to rotate in and out of view. This may also be capturing acute changes in the He-10830 absorption strength due to flaring (particularly for V1298 Tau). This timescale of increased variability might be due to the lifetime of the helium metastable state, which is 2.2 hours (Drake 1971). The changing He-10830 absorption strength on this relatively short timescale of $\Delta t \sim 5$ hr may represent de- and re-population of the helium metastable state between observations. Above timescales of $\Delta t \sim 5$ hr, the EW difference plateau represents variability in the He-10830 absorption strength (e.g. from active regions, flares) that is averaged out over multiple epochs.

4.3.1. *Short timescales: intra-night variability*

We can also assess variability on the shortest timescales by inspecting measurements taken on the same night. In our observing strategy, an observation of a target is composed of multiple consecutive exposures (normally 3). This results in multiple spectra separated by $5 - 10$ minutes. Figure 11 shows the intra-visit EW[He] variability, representing the shortest timescales of $\lesssim 30$ minutes, as a function of age. We quantify the intra-visit variability by computing the absolute EW difference between each pair of observations in a single visit, and then present the median pairwise difference

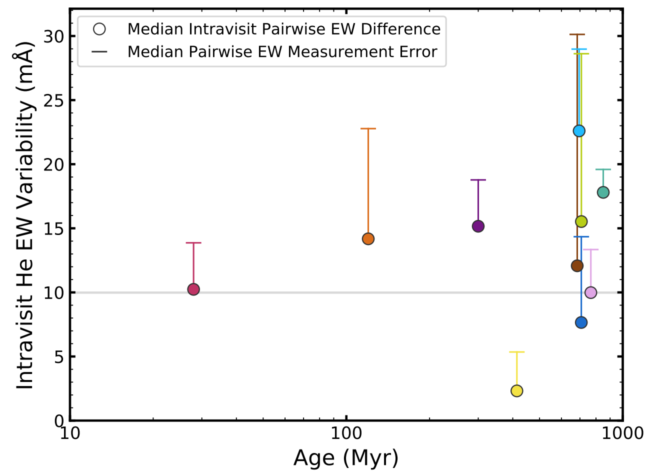

Figure 11. Intra-visit variability of EW[He] to demonstrate variability within baselines of 30 minutes as a function of age. The plotted ages for the Hyades and Praesepe members are artificially spread to avoid overlapping points. At these shortest timescales, the variability is independent of age, giving confidence that detecting even the youngest exospheres is possible with comparison observations directly surrounding transit. The typical measurement errors for each object are plotted as the horizontal line markers, and are all larger than the variability values.

for each target. This is directly comparable to exosphere detections which are presented as measurements of excess absorption depth (essentially differences in EW). We also plot the typical measurement error on an object's pairwise EW difference, from adding in quadrature individual measurement errors.

The intra-visit variability has no dependence on age, unlike the long-term averaged variability. This agrees with our conclusion from the "EW difference power spectra" (Figure 10) that variability is smaller on shorter timescales, and that it is age-independent at the shortest timescales. This is promising for the detection of young exospheres if out-of-transit observations are taken directly surrounding transit.

The typical measurement error is larger than the intra-visit variability for all objects, so we cannot measure the "intrinsic" intra-visit variability. The intra-visit variability has a comparable amplitude to the long-term time-averaged variability for our sample with $\tau \gtrsim 300$ Myr, although the two quantities are not quite statistically comparable. We note that HD 63433, which is by far the brightest target in our sample, has significantly smaller intra-visit variability than the rest of the sample despite having comparable long-term time-averaged variability. With it's higher S/N, this means that HD 63433's value is closer to the "intrinsic" intra-visit variability which is indeed smaller than the long-term time-averaged variability. This also gives us confidence that higher S/N from stacked spectra taken across the transit will increase the reliability of exosphere observations.

However, there still could be increased variability on short timescales. The He-10830 triplet strength increases from flares (Fuhrmeister et al. 2020), which act on timescales of minutes to hours. Vissapragada et al. (2021) even found a linear increase in the He-10830 triplet strength of V1298 Tau in the decay phase of a flare, potentially indicating the line's temporal response. The observation was during a transit of V1298 Tau c, though, so the increase could have been due to either the flare or an exosphere. Other acute active phenomena could change the He-10830 triplet strength, such as spot/plage rotation, chromospheric network variability, winds, and mass loss. While variability is small on timescales that cover out-of-transit observations directly surrounding transit, care still must be taken when interpreting He-10830 triplet transit observations in the context of stellar activity.

4.3.2. *Intermediate timescales: intensive observing campaigns*

We further investigate variability in the He-10830 absorption strength at intermediate timescales using the intensive campaigns that were taken for three targets in our sample: V1298 Tau, K2-136, and K2-100. These intensive campaigns include regular observations over a months-long span, with individual visits often only separated by a day. The high cadence of these data is useful to search for periodicity, unlike the sparse, years-long time series for most targets in our sample. More frequent observations are also more likely to catch acute changes in the He-10830 absorption such as from flares. We computed periodograms for each intensive time series to search for periodicity, and discuss these observations below.

V1298 Tau: With the highest EW[He] variability in our sample, V1298 Tau provides an important opportunity to study significant absorption strength changes at high cadence. V1298 Tau is a unique system: it is a very young ($\tau \sim 25$ Myr) early K-dwarf, hosts 4 known transiting planets (David et al. 2019b,a), is a promising candidate for follow-up atmospheric characterization of young planets, and is a useful probe of star and planet formation as a member of the older distributed stellar groups around Taurus (Krolikowski et al. 2021). The intensive campaign for V1298 Tau comprises 30 visits (98 spectra) spanning 45 days, with a median visit separation of 1 day. There was a brief break in observations for 12 days in the middle of the campaign. This intensive campaign was taken in October-November of 2019 with the goal of measuring the mass of V1298 Tau b, which will be presented in a future paper. Figure 12 shows the intensive EW[He] time series of V1298 Tau, which features significant structure. The EW[He] varies by almost 300 mÅ in the first week and a half of the intensive campaign, before settling down to vary by ~ 100 mÅ around a stable value, and then dropping further in the last few days. There is also an observation with greatly elevated EW[He] at JD ~ 2458786 that may be indicative of a flare.

There is no significant periodicity across the entire time series, which may indicate that the variability in the He-10830 absorption strength comes from equal spatial distribution of active regions across the surface, such as extreme spot coverage and the chromospheric network. However, there *is* significant periodicity near the stellar rotation period within the first week and a half of the campaign when the absorption varies wildly. The periodogram of the first week and a half of data is shown in the top panel of Figure 13. The bottom panel of Figure 13 shows the intensive campaign phased to the period of peak periodogram power, and the data from the first week and a half is coherent unlike the rest of the time series.

This contradicts the conclusion from the entire intensive data set that variability is essentially smeared out across the stellar rotation. We posit that the large amplitude variation at the stellar rotation period may be from an extreme flaring or mass loss event that created a large but spatially concentrated bright spot on the stellar chromosphere, which would then show enhanced He-10830 absorption when it rotates into view. This highlights the volatility in EW[He] at such high activity levels, and warrants even further caution for planning time sensitive transit observations.

K2-136: K2-136 is a K5.5-dwarf Hyades member that hosts 3 transiting planets (Mann et al. 2018; Ciardi et al. 2018; Livingston et al. 2018), and is representative of the older targets in our sample that have He-10830 variability in line with the field. It has a rotation period on the slower end of our sample's range (15 days), with 7 of the 10 stars having faster rotation. The intensive campaign for K2-136 comprises 22 visits (68 spectra) spanning 80 days, with a median visit separation of 2 days. There was a brief break in observations for 20 days in the middle of the campaign. This intensive campaign was observed soon after HPF's commissioning, and has been used as a standard reference by our team in analyzing HPF data. The top panel of Figure 14 shows the intensive EW[He] time series of K2-136, which is fairly flat over the course of the observations. It is unsurprising that an older, less active star would show less structure in the high cadence EW[He] measurements. The intensive campaign has periodicity near the stellar rotation period, shown by the periodogram in the bottom panel of Figure 14, but it has power just barely above the 1% false alarm probability level. This potential rotational modulation is inconclusive, and we do not show the phased time series because it does not show clear modulation. The average EW during the intensive campaign is lower than for the rest of the sparse time series, which may be indicative of longer term (months to years-long) activity cycles manifesting in the EW[He] of K2-136.

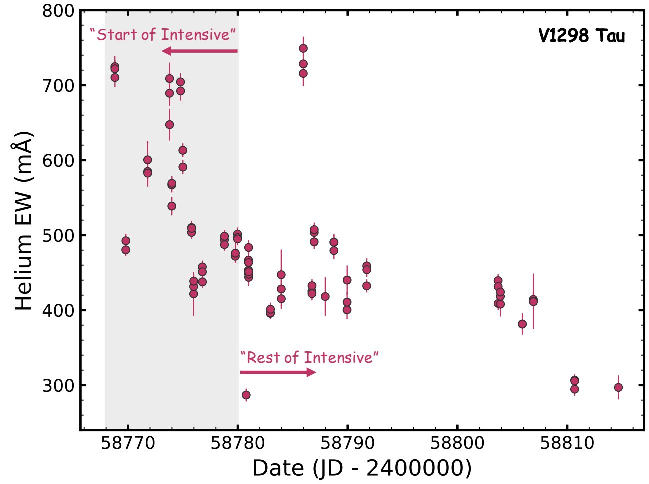

Figure 12. The EW[He] time series for the V1298 Tau intensive campaign. In the first week and a half of the campaign, there is extreme variability in the EW value, which then steadies at a slightly lower value for the remaining time series coverage.

K2-100: K2-100 is an F6-dwarf Praesepe member that hosts a transiting planet (Mann et al. 2017), and features the fastest rotation period in our sample besides the much younger V1298 Tau. However, it has He-10830 absorption strength and variability comparable to the rest of the "older" targets in our sample. The intensive campaign for K2-100 comprises 24 vis-

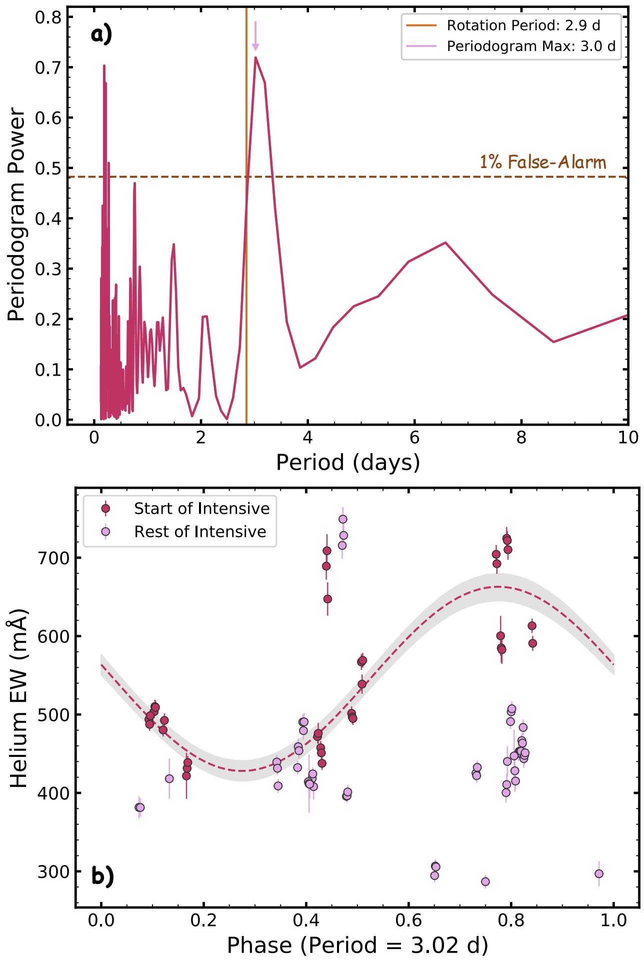

Figure 13. Periodicity analysis of the V1298 Tau intensive campaign. *Top Panel:* The periodogram of the first week and a half of data from the intensive campaign, which features extreme variability. The peak of the periodogram ($P = 3.02$ d) is very close to the rotation period of the star ($P = 2.9$ d), and has power well above the 1% false alarm probability level. *Bottom panel:* The intensive campaign phased to the periodogram peak's period, shown for the first week and a half separately from the rest of the intensive time series data. The coherence at the start of the campaign is stark, while there is no apparent rotational modulation for the data from the remainder of the campaign.

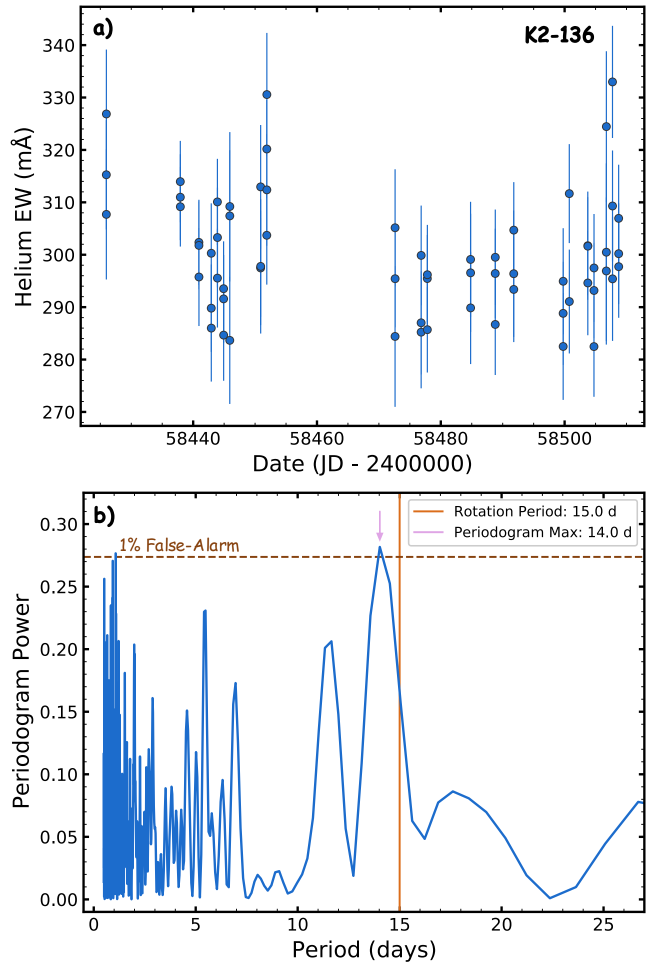

Figure 14. *Top Panel:* The EW[He] time series for the K2-136 intensive campaign. The data is fairly flat, and most of the variability shown is within the individual EW measurement uncertainties. *Bottom panel:* The periodogram for the full intensive campaign of K2-136, which shows a peak that is significant just above the 1% false alarm probability level. The period of the peak ($P = 14$ d) is close to the stellar rotation period ($P = 15$ d). Given the power of the peak, the periodicity found here is taken to be inconclusive.

its (72 spectra) spanning 80 days, with a median visit separation of 1 day. There are two brief 16-day breaks in the observations in the middle of the campaign. This intensive campaign was taken to measure the mass of K2-100b, which will be presented in a future paper. Figure 15 shows the intensive EW[He] time series of K2-100, which is fairly flat over the course of the observations, similarly to K2-136. Interestingly, there are no significant periodicities found for this data set. We may have expected rotational modulation due to its faster rotation period than K2-136, but this may be indicative of

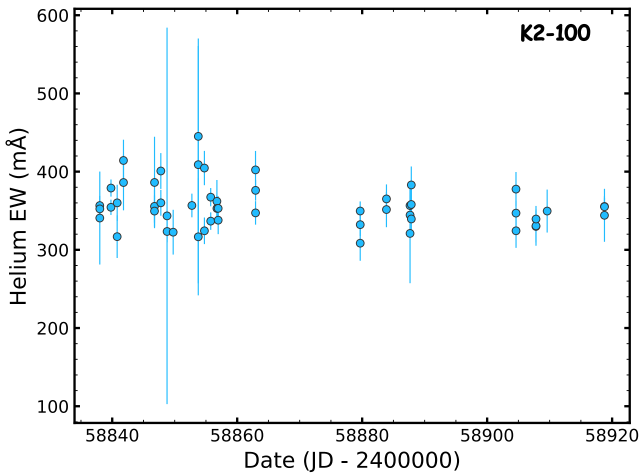

Figure 15. The EW[He] time series for the K2-100 intensive campaign. The data is fairly flat, and most of the variability shown is within the individual EW measurement uncertainties.

rotationally-smeared He-10830 absorption from the general chromospheric network or spatially distributed surface active regions.

For completeness, we compute the periodogram power spectra of all targets' full time series and see no significant periodicity, which is not surprising given their sparse cadence. In all, we only see any amount of rotational modulation in two targets: V1298 Tau with significant modulation over just one week and a half of the observations, and K2-136 with a periodigram power that is barely significant. While the He-10830 absorption strength variability seems to be dependent on the stellar age, and thus activity level and volatility, there is no significant relation between the He-10830 variability and stellar rotation. This may indicate that He-10830 line formation is not solely tied to spot or plage features, which are typically visualized as producing rotationally modulated stellar activity signals. Instead, He-10830 may be formed from those active regions, in addition to the broader active chromospheric network that essentially smears the He-10830 absorption changes across the stellar surface.

5. IMPLICATIONS FOR THE DETECTION OF YOUNG EXOSPHERES

With the intrinsic stellar variability of the He-10830 triplet at young ages quantified, we can assess the feasibility of detecting young helium exospheres and the effects stellar activity may have on these observations. The stellar He-10830 triplet is demonstrably sensitive to activity, and intrinsic absorption changes could masquerade as an exosphere signal. The amplitude of the planetary He-10830 triplet absorption signal is set by the exosphere's metastable helium population and the atmospheric mass loss rate, both of which depend on the activity-sensitive high-energy radiative output of the host star (Oklopčić 2019; Poppenhaeger 2022). In this section, we discuss the feasibility of detecting young helium exospheres in light of stellar variability, and explore scenarios in which activity may affect exosphere observations.

To assess the degree to which changes in the stellar He-10830 triplet may be confused with an exosphere's signal, we compare the intrinsic EW[He] variability for our sample to exosphere observations with high resolution spectra from the literature. Figure 16 shows helium exosphere detections and upper limits, as percentage excess absorption depths, with our measurements of intrinsic stellar variability plotted as horizontal lines. We show the long-term time-averaged "intrinsic" variability quantities (with measurement error deconvolved) converted to percent-depths relative to each target's median EW[He]. To visualize the age dependence, we separately plot the variability of V1298 Tau to represent the youngest and most active stars, an average of all older objects to represent ages when variability approaches the field's, and K2-284 to represent ages between these two extremes. These quantities are not *quite* comparable to exosphere observations, because exosphere detections are presented as the peak excess absorption as opposed to our EWs which

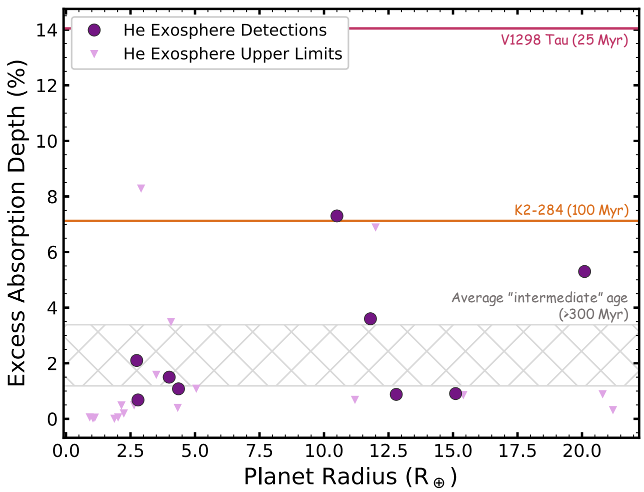

Figure 16. Literature helium exosphere detections (circles) and upper limits (triangles) compared to the intrinsic stellar variability in the line. We convert the long-term, time-averaged intrinsic EW[He] variability (with measurement error deconvolved) to percentages relative to the median EW value for each target. To show the age dependence, we plot the variability of V1298 Tau and K2-284 as horizontal lines, and the range of variability for the older objects as the gray hatched region. The exosphere detections are all smaller than variability at the youngest ages, but by 300 Myr the intrinsic stellar variability should not preclude exosphere detection.

integrate over the entire feature. Our measurements are equivalent to the peak excess absorption if only the depth, and not width, is changing. However, the quantities are similar enough for comparing the amplitudes of each signal.

All currently detected helium exospheres have depths smaller than V1298 Tau's variability, and all but one are shallower than K2-284's variability. From this, we conclude that comparing spectra from across observing seasons (even separated by days) is inadequate for detecting helium exospheres at ages below 100 Myr. At ages older than 300 Myr, the range in variability is comparable to, if not smaller than, all exosphere detections. "Older" helium exospheres should be detectable even with observations spanning an observing season, notwithstanding spurious signals caused by inopportune timing of activity events (e.g. flares). Stellar variability may be large enough to preclude detection at the youngest ages ($\tau \lesssim 100$ Myr), but we are confident that it will *not* necessarily preclude detection at ages of $\tau \gtrsim 300$ Myr.

There are important caveats to discuss that positively impact the potential detection of young helium exospheres. We so far discuss the *long-term, time-averaged* variability, which represents the typical difference in EW from the median value averaged across long observation baselines. Crucially, we show in Section 4.3 that EW[He] variability is smaller than average at the shortest timescales ($\Delta t \lesssim 5$ hr) and not age-dependent. Out-of-transit observations directly surrounding transit should further decrease the prospect of activity-driven confusion in interpreting results. Also, there are reasons why young exosphere signals may be larger than older counterparts. Young stars have greater high-energy radiative output, which should increase both the exosphere's metastable helium population (leading to more He-10830 triplet absorption; Oklopčić 2019; Poppenhaeger 2022) and atmospheric mass loss rate (Lopez et al. 2012; Lopez & Fortney 2013; Owen & Wu 2017).

5.1. *Scenarios where activity may still affect exosphere observations*

There are still situations in which stellar activity-driven variability in the He-10830 triplet could complicate exosphere detection. In particular, we are concerned with scenarios where the timescales of stellar variability and exosphere observations overlap. Below, we discuss four scenarios that may affect the detection of young exospheres, although this list is hardly exhaustive and meant to be emblematic of potential issues with the He-10830 triplet.

1) Flares: Stellar He-10830 triplet absorption is enhanced by flares (Andretta et al. 2008; Sanz-Forcada & Dupree 2008; Kobanov et al. 2018). If a flare occurs near transit, there may be an increase in the He-10830 triplet absorption strength that could be interpreted as an exosphere, despite being stellar in nature. This would be most likely for very young stars that feature the greatest flare rates. In our sample this includes V1298 Tau, for which Vissapragada et al. (2021) observed a flare during the transit of one of its planets, and could not distinguish between the flare or an exosphere as the cause for increased absorption. Flares could also increase the atmospheric mass loss rate (Wang & Dai 2021), leading to an increase in the exosphere He-10830 triplet absorption lagged from the flare by a few hours. In that case, enhanced absorption would be a result of *both* the star and the exosphere. It may be possible to disentangle these signals given the lifetime of each, but the temporal response of the stellar He-10830 triplet feature to a flare is unknown.

2) Lack of rotational coherence: We find nearly no significant signals at the stellar rotation period in our data, implying that changes in the He-10830 triplet absorption are not rotationally coherent (particularly for longer than a few rotations). This could be detrimental to exosphere detection, as the activity-induced variability could not be modeled at the known rotation period and subtracted. This also means that the He-10830 triplet could not be Doppler mapped to identify distinct causative active regions. Other traditional spectral activity indicators that do correlate with rotation may not track changes in the He-10830 triplet, and thus could not be used in models of activity's effect on the He-10830 triplet.

3) Longer baseline out-of-transit comparison: Out-of-transit comparison spectra may simply need to be taken further separated from mid-transit than the $\sim$ 5 hr timescale of increased intrinsic stellar He-10830 absorption variability. One reason could be a transit that is on the order of or longer than this timescale. The median transit duration of the known young transiting planets is 3.2 hr and the longest duration is 7.5 hr. Extended out-of-transit baseline could be long enough from parts of the transit when stellar variability may introduce changes in the He-10830 absorption strength. Depending on the transit timing, object visibility, and observing conditions, it might be necessary to obtain out-of-transit comparison spectra on a different night, which is more susceptible to activity contamination. This also would affect comparing absorption depth changes across multiple transits.

4) Exosphere structure: An extended exosphere may affect its own detection, particularly for a tail-like structure that effectively increases the helium transit duration compared to the white-light transit. Tails created by atmospheric mass loss have long been predicted (Schneider et al. 1998), and have now been observed in helium gas for multiple planets (Nortmann et al. 2018; Alonso-Floriano et al. 2019; Spake et al. 2021). Bow shocks and up-orbit accretion flows could also produce a "leading tail" (Matsakos et al. 2015), which has been observed for one helium exosphere (Czesla et al. 2022). By lengthening the transit, these extended exospheres increase the likelihood of activity-induced variability occurring during transit observations, as explained in point 3 above. Such a scenario would complicate the definition of "out-of-transit" observations, and necessitate more baseline observations further from transit. One can imagine an extreme situation of a compact multi-planet system where tails from multiple planets could lead to overlapping extended transits (e.g. TRAPPIST-1, although no helium exosphere was detected for 3 of its planets; Krishnamurthy et al. 2021). This would result in a "constant" presence of helium exosphere material in the system. While this situation is not necessarily common, such multi-planet systems (like V1298 Tau) are being observed, so it is plausible enough to encourage care when considering the timing of transit observations.

5.2. *Companion observations for planning campaigns and mitigating He variability*

A reconnaissance NIR spectrum to measure the EW[He] of planet hosts would help to prioritize targets for exosphere observing campaigns. High EW[He] itself, which is enhanced by stellar activity, could indicate a higher likelihood of a detectable helium exosphere. Activity is accompanied by greater stellar high-energy radiative output, which would excite more metastable helium in the exosphere to produce a deeper planetary absorption signal. EW[He] is less informative for active stars with $\tau \gtrsim 300$ Myr, though, because the absorption strength saturates at intermediate ages. The EW[He] reconnaissance may be more useful for older, less active stars where the PR mechanism (and thus coronal radiation) will dominate the metastable helium excitation. It is important to note that activity in the youngest stars *also* indicates increased stellar variability, which would impede exosphere observations. Regardless, stronger He-10830 absorption of a host star may be useful as an indicator for the likelihood of a detectable helium exosphere.

There are also companion observations that could help to mitigate contamination of exosphere observations from stellar activity-driven variability. Extended out-of-transit monitoring would establish a more reliable baseline stellar He-10830 absorption strength, and could be used to identify the timescale and amplitude of intrinsic stellar variability. Long-term monitoring could also be used to distinguish between periods of increased and decreased variability for planning observations (as we see in Section 4.3.2). Ideally, one would observe consecutive transits with baseline observations taken before the first transit through after the last transit. This would provide a long baseline for comparison, as well as multiple transits to increase the reliability of any detection. Simultaneous photometry could be used to monitor for strong flares that may affect the stellar absorption near transit, as was done for an observation of V1298 Tau by Vissapragada et al. (2021).

Beyond this, further studies of the stellar He-10830 triplet are needed to connect the feature to established activity proxies that may help detrend the intrinsic stellar variability in the line. An enlarged sample of stars at younger ages (particularly between 50 and 300 Myr) would further establish the behavior of the He-10830 triplet in youth and the feasibility of exosphere detections.

6. CONCLUSIONS AND FUTURE WORK

Young planets hold unique potential to better our understanding of the formation and evolution of exoplanet atmospheres. Since its mission began, TESS has followed K2 in discovering young planetary systems around bright stars that are well-suited for atmospheric characterization. Critically, some of these systems have been found in new stellar associations with ages between 100 and 400 Myr (e.g. Newton et al. 2021; Tofflemire et al. 2021; Hedges et al. 2021; Dong et al. 2022, Newton et al. submitted). With the continued use of precision NIR spectrographs, the He-10830 triplet will persist as a crucial probe of the mass loss from these young planets. These follow-up observations will require knowledge of the intrinsic stellar variability of the He-10830 triplet because the host stars have high activity levels.

In this paper, we present an initial study of the He-10830 triplet in youth using unique NIR spectroscopic data from HPF for a subset of the known young transiting planet hosts. We measured the He-10830 triplet absorption strength and variability of our sample to characterize the feature's relationship with stellar activity, and discussed implications for exosphere detections. To summarize our results:

1. We developed a self-calibration technique to subtract strong telluric sky emission lines from HPF spectra, which are not adequately subtracted using just the sky fiber spectra. This is important as there is a very strong sky line that can overlap the He-10830 triplet, making it harder to measure the feature's absorption strength.

2. We find that the EW[He] is enhanced for young stars relative to inactive dwarfs. There is no effective temperature dependence, but there is a relation with stellar rotation period: there is stronger absorption at shorter rotation periods. While all of our stars are young, activity levels are higher at the youngest ages and most rapid rotation. Despite a likely significant difference in the high-energy radiative output of our sample, we find a plateau in EW[He] from $P_{\rm rot} \sim 5-20$ days. We conclude that in young and active chromospheres, metastable helium is populated primarily through collisional excitation, and that contributions from the PR mechanism only appear at the high and low relative activity regimes.

3. The intrinsic stellar variability in EW[He] is large at young ages ($\tau \lesssim 100$ Myr), and decreases to a plateau comparable to the expected field variability at $\tau \gtrsim 300$ Myr. This variability is caused by volatility and evolution of the stellar activity level, such as by flares or changing surface heterogeneities, which is most common at the youngest ages.

4. The intrinsic stellar EW[He] variability is smallest on the shortest timescales (an hour), giving us confidence for detecting young exospheres with immediate out-of-transit comparison observations. However, the variability increases within just 5 hours for the youngest star in our sample (V1298 Tau) and within a day for the rest of the sample, perhaps from the coherence of flare-induced absorption changes. Comparing spectra of young stars from night-to-night may introduce stellar variability that can mask or masquerade as an exosphere signal. The convolution of stellar and planetary signals must be considered when longer baseline out-of-transit observations are taken, particularly if the exosphere has extended structure, such as a tail.

5. We find little evidence for periodicity with the stellar rotation in EW[He] implying that the chromospheric regions in which the line forms are not rotationally localized. We do, however, see stellar rotation periodicity within the first week and a half of a month-long intensive campaign of V1298 Tau, featuring extreme absorption strength changes. The He-10830 triplet is most variable and complicated at the youngest ages, and may have rotational modulation during extreme flaring events or in the presence of large, persistent high contrast surface heterogeneities.

6. Youth does not necessarily preclude the detection of helium exospheres given the low intrinsic variability in the He-10830 triplet at the shortest timescales, even at the youngest ages. However, there may still be confusion between enhanced absorption from exospheres and stellar active regions or flares. Care must be taken when searching for exosphere signals when observations are separated by longer than a few hours, as variability can be significant on timescales greater than a day. Continuous spectroscopic and photometric monitoring around transit would help to mitigate the deleterious effect of stellar activity.

Our understanding of the He-10830 triplet of young and active stars is still incomplete. More targets must be observed and uniformly analyzed to cover our sample's gaps in age, spectral type, rotation period, and activity level. Mapping EW[He] at more densely sampled stellar parameters, particularly rotation period, would further elucidate the origin of the line in young chromospheres. Only two of our targets are young enough to feature enhanced He-10830 triplet variability. More young targets ($\tau \lesssim$ 300 Myr) are needed to robustly assess the feasibility of detecting young exospheres and determine variability timescales that help to best plan observing campaigns. Additionally, intensive campaigns of a select few highly active stars could be used to search for activity cycles and rotational coherence in EW[He].

Other observations that are contemporaneous with NIR spectroscopy would complement the conclusions we draw about the He-10830 triplet in youth. Photometric monitoring could assist in connecting He-10830 triplet variability to spot modulation and evolution, and search for rotational or long-term cyclic modulation in the He-10830 triplet. X-ray or UV observations would provide instantaneous measurements of the high-energy coronal radiation that may drive the excitation of the helium metastable state, and definitively distinguish contributions from the PR and CE mechanisms. Visible spectroscopy would provide measurements of established chromospheric activity indicators (such as Ca II H and K, and H-α), mapping lines that are formed at varying chromospheric heights and tying helium variability to well-studied probes of activity.

NIR precision RV measurements are still new, and there are no well-established activity indicators in the NIR bandpass that are analogous to Ca II H and K in the visible. The lack of rotational coherence in our observations of the He-10830 triplet calls into question whether or not it would work well as an activity indicator to de-trend RV jitter. It may provide information about second-order activity effects on the stellar spectral line profile, but may not be able to act alone as a NIR activity indicator for precision RV studies. An in-depth analysis connecting EW[He] to RVs for our sample is beyond the scope of this paper, but will be featured in a future work.

Time series studies of young exoplanet hosts provide crucial data for understanding young stellar structure, planet formation and evolution, and the effects of stellar activity on exoplanet observations. In particular, the recent developments in NIR precision spectroscopy have opened an entirely new window into studies of stars and exoplanets, but the results of these ongoing programs are nascent (Reiners et al. 2018; Donati et al. 2020; Tran et al. 2021). With advancements in panchromatic observing capabilities, it is ever more pressing to expand the frontiers of stellar astrophysics to best understand the manifestation of stellar activity in extreme precision exoplanet observations.

Facility: HET (HPF)

Software: Astropy (Astropy Collaboration et al. 2013, 2018), barycorrpy (Kanodia & Wright 2018), ipython (Perez & Granger 2007), jupyter (Kluyver et al. 2016), matplotlib (Hunter 2007), NumPy (van der Walt et al. 2011), pandas (Reback et al. 2020), SciPy (Virtanen et al. 2020), TelFit (Gullikson et al. 2014)

REFERENCES

Allart, R., Bourrier, V., Lovis, C., et al. 2018, Science, 362, 1384, doi: 10.1126/science.aat5879

Alonso-Floriano, F. J., Snellen, I. A. G., Czesla, S., et al. 2019, A&A, 629, A110, doi: 10.1051/0004-6361/201935979

Andretta, V., & Giampapa, M. S. 1995, ApJ, 439, 405, doi: 10.1086/175183

Andretta, V., Giampapa, M. S., Covino, E., Reiners, A., & Beeck, B. 2017, ApJ, 839, 97, doi: 10.3847/1538-4357/aa6a14

Andretta, V., & Jones, H. P. 1997, ApJ, 489, 375, doi: 10.1086/304760

Andretta, V., Mauas, P. J. D., Falchi, A., & Teriaca, L. 2008, ApJ, 681, 650, doi: 10.1086/587933

Astropy Collaboration, Robitaille, T. P., Tollerud, E. J., et al. 2013, A&A, 558, A33, doi: 10.1051/0004-6361/201322068

Astropy Collaboration, Price-Whelan, A. M., Sipőcz, B. M., et al. 2018, AJ, 156, 123, doi: 10.3847/1538-3881/aabc4f

Avrett, E. H. 1998, in Solar Electromagnetic Radiation Study for Solar Cycle 22, ed. J. M. Pap, C. Frohlich, & R. K. Ulrich, 449

Avrett, E. H., Fontenla, J. M., & Loeser, R. 1994, in Infrared Solar Physics, ed. D. M. Rabin, J. T. Jefferies, & C. Lindsey, Vol. 154, 35

Baliunas, S. L., Donahue, R. A., Soon, W. H., et al. 1995, ApJ, 438, 269, doi: 10.1086/175072

Boldt, S., Oshagh, M., Dreizler, S., et al. 2020, A&A, 635, A123, doi: 10.1051/0004-6361/201937419

Boro Saikia, S., Lüftinger, T., Folsom, C. P., et al. 2022, A&A, 658, A16, doi: 10.1051/0004-6361/202141525

Bourrier, V., Lecavelier des Etangs, A., Ehrenreich, D., et al. 2018, A&A, 620, A147, doi: 10.1051/0004-6361/201833675

Brajša, R., Pohjolainen, S., Ruždjak, V., et al. 1996, SoPh, 163, 79, doi: 10.1007/BF00165457

Brandt, T. D., & Huang, C. X. 2015, ApJ, 807, 24, doi: 10.1088/0004-637X/807/1/24

Ciardi, D. R., Crossfield, I. J. M., Feinstein, A. D., et al. 2018, AJ, 155, 10, doi: 10.3847/1538-3881/aa9921

Czesla, S., Lampón, M., Sanz-Forcada, J., et al. 2022, A&A, 657, A6, doi: 10.1051/0004-6361/202039919

David, T. J., Petigura, E. A., Luger, R., et al. 2019a, ApJL, 885, L12, doi: 10.3847/2041-8213/ab4c99

David, T. J., Conroy, K. E., Hillenbrand, L. A., et al. 2016, AJ, 151, 112, doi: 10.3847/0004-6256/151/5/112

David, T. J., Mamajek, E. E., Vanderburg, A., et al. 2018, AJ, 156, 302, doi: 10.3847/1538-3881/aaeed7

David, T. J., Cody, A. M., Hedges, C. L., et al. 2019b, AJ, 158, 79, doi: 10.3847/1538-3881/ab290f

Desort, M., Lagrange, A. M., Galland, F., Udry, S., & Mayor, M. 2007, A&A, 473, 983, doi: 10.1051/0004-6361:20078144

Donati, J. F., Kouach, D., Moutou, C., et al. 2020, MNRAS, 498, 5684, doi: 10.1093/mnras/staa2569

Dong, J., Huang, C. X., Zhou, G., et al. 2022, ApJL, 926, L7, doi: 10.3847/2041-8213/ac4da0

Douglas, S. T., Agüeros, M. A., Covey, K. R., et al. 2014, ApJ, 795, 161, doi: 10.1088/0004-637X/795/2/161

Drake, G. W. 1971, PhRvA, 3, 908, doi: 10.1103/PhysRevA.3.908

Dring, A. R., Linsky, J., Murthy, J., et al. 1997, ApJ, 488, 760, doi: 10.1086/304738

Dupree, A. K., Sasselov, D. D., & Lester, J. B. 1992, ApJL, 387, L85, doi: 10.1086/186311

Ehrenreich, D., Lecavelier Des Etangs, A., & Delfosse, X. 2011, A&A, 529, A80, doi: 10.1051/0004-6361/201016162

Ehrenreich, D., Bourrier, V., Bonfils, X., et al. 2012, A&A, 547, A18, doi: 10.1051/0004-6361/201219981

Feinstein, A. D., David, T. J., Montet, B. T., et al. 2022, ApJL, 925, L2, doi: 10.3847/2041-8213/ac4745

Feinstein, A. D., Montet, B. T., Johnson, M. C., et al. 2021, AJ, 162, 213, doi: 10.3847/1538-3881/ac1f24

Fuhrmeister, B., Czesla, S., Hildebrandt, L., et al. 2019, A&A, 632, A24, doi: 10.1051/0004-6361/201936193

—. 2020, A&A, 640, A52, doi: 10.1051/0004-6361/202038279

Fulton, B. J., Petigura, E. A., Howard, A. W., et al. 2017, AJ, 154, 109, doi: 10.3847/1538-3881/aa80eb

Gaidos, E., Hirano, T., Omiya, M., et al. 2021, Research Notes of the American Astronomical Society, 5, 238, doi: 10.3847/2515-5172/ac31bd

Gaidos, E., Mann, A. W., Rizzuto, A., et al. 2017, MNRAS, 464, 850, doi: 10.1093/mnras/stw2345

Gaidos, E., Hirano, T., Mann, A. W., et al. 2020a, MNRAS, 495, 650, doi: 10.1093/mnras/staa918

Gaidos, E., Hirano, T., Wilson, D. J., et al. 2020b, MNRAS, 498, L119, doi: 10.1093/mnrasl/slaa136

Gaidos, E., Hirano, T., Beichman, C., et al. 2022, MNRAS, 509, 2969, doi: 10.1093/mnras/stab3107

Ginzburg, S., Schlichting, H. E., & Sari, R. 2018, MNRAS, 476, 759, doi: 10.1093/mnras/sty290

Goldberg, L. 1939, ApJ, 89, 673, doi: 10.1086/144092

Gossage, S., Conroy, C., Dotter, A., et al. 2018, ApJ, 863, 67, doi: 10.3847/1538-4357/aad0a0

Gullikson, K. 2014, TelFit: Fitting the telluric absorption spectrum. http://ascl.net/1405.002

Gullikson, K., Dodson-Robinson, S., & Kraus, A. 2014, AJ, 148, 53, doi: 10.1088/0004-6256/148/3/53

Hartmann, L., Davis, R., Dupree, A. K., et al. 1979, ApJL, 233, L69, doi: 10.1086/183078

Hearty, F., Levi, E., Nelson, M., et al. 2014, in Society of Photo-Optical Instrumentation Engineers (SPIE) Conference Series, Vol. 9147, Ground-based and Airborne Instrumentation for Astronomy V, ed. S. K. Ramsay, I. S. McLean, & H. Takami, 914752, doi: 10.1117/12.2056720

Hedges, C., Hughes, A., Zhou, G., et al. 2021, AJ, 162, 54, doi: 10.3847/1538-3881/ac06cd

Hirano, T., Krishnamurthy, V., Gaidos, E., et al. 2020, ApJL, 899, L13, doi: 10.3847/2041-8213/aba6eb

Hunter, J. D. 2007, Computing in Science and Engineering, 9, 90, doi: 10.1109/MCSE.2007.55

Husser, T. O., Wende-von Berg, S., Dreizler, S., et al. 2013, A&A, 553, A6, doi: 10.1051/0004-6361/201219058

Ikoma, M., & Hori, Y. 2012, ApJ, 753, 66, doi: 10.1088/0004-637X/753/1/66

Jackson, A. P., Davis, T. A., & Wheatley, P. J. 2012, MNRAS, 422, 2024, doi: 10.1111/j.1365-2966.2012.20657.x

Jin, S., Mordasini, C., Parmentier, V., et al. 2014, ApJ, 795, 65, doi: 10.1088/0004-637X/795/1/65

Johnson, M. C., David, T. J., Petigura, E. A., et al. 2022, AJ, 163, 247, doi: 10.3847/1538-3881/ac6271

Johnstone, C. P., Güdel, M., Stökl, A., et al. 2015, ApJL, 815, L12, doi: 10.1088/2041-8205/815/1/L12

Kanodia, S., & Wright, J. 2018, Research Notes of the American Astronomical Society, 2, 4, doi: 10.3847/2515-5172/aaa4b7

Kaplan, K. F., Bender, C. F., Terrien, R. C., et al. 2019, in Astronomical Society of the Pacific Conference Series, Vol. 523, Astronomical Data Analysis Software and Systems XXVII, ed. P. J. Teuben, M. W. Pound, B. A. Thomas, & E. M. Warner, 567

Katsova, M. M., & Shcherbakov, A. G. 1998, A&A, 329, 1080

Kluyver, T., Ragan-Kelley, B., Pérez, F., et al. 2016, in Positioning and Power in Academic Publishing: Players, Agents and Agendas, ed. F. Loizides & B. Scmidt (IOS Press), 87–90. https://eprints.soton.ac.uk/403913/

Kobanov, N., Chelpanov, A., & Pulyaev, V. 2018, Journal of Atmospheric and Solar-Terrestrial Physics, 173, 50, doi: 10.1016/j.jastp.2018.04.007

Kramida, A., Yu. Ralchenko, Reader, J., & and NIST ASD Team. 2021, NIST Atomic Spectra Database (ver. 5.9), [Online]. Available: `https://physics.nist.gov/asd` [2022, May 13]. National Institute of Standards and Technology, Gaithersburg, MD.

Krishnamurthy, V., Hirano, T., Stefánsson, G., et al. 2021, AJ, 162, 82, doi: 10.3847/1538-3881/ac0d57

Krolikowski, D. M., Kraus, A. L., & Rizzuto, A. C. 2021, AJ, 162, 110, doi: 10.3847/1538-3881/ac0632

Kubyshkina, D., Lendl, M., Fossati, L., et al. 2018, A&A, 612, A25, doi: 10.1051/0004-6361/201731816

Lammer, H., Selsis, F., Ribas, I., et al. 2003, ApJL, 598, L121, doi: 10.1086/380815

Lammer, H., Stökl, A., Erkaev, N. V., et al. 2014, MNRAS, 439, 3225, doi: 10.1093/mnras/stu085

Lecavelier Des Etangs, A., Ehrenreich, D., Vidal-Madjar, A., et al. 2010, A&A, 514, A72, doi: 10.1051/0004-6361/200913347

Liu, S.-F., Hori, Y., Lin, D. N. C., & Asphaug, E. 2015, ApJ, 812, 164, doi: 10.1088/0004-637X/812/2/164

Livingston, J. H., Dai, F., Hirano, T., et al. 2018, AJ, 155, 115, doi: 10.3847/1538-3881/aaa841

Lopez, E. D., & Fortney, J. J. 2013, ApJ, 776, 2, doi: 10.1088/0004-637X/776/1/2

Lopez, E. D., Fortney, J. J., & Miller, N. 2012, ApJ, 761, 59, doi: 10.1088/0004-637X/761/1/59

Mahadevan, S., Ramsey, L., Bender, C., et al. 2012, in Society of Photo-Optical Instrumentation Engineers (SPIE) Conference Series, Vol. 8446, Ground-based and Airborne Instrumentation for Astronomy IV, ed. I. S. McLean, S. K. Ramsay, & H. Takami, 84461S, doi: 10.1117/12.926102

Mahadevan, S., Ramsey, L. W., Terrien, R., et al. 2014, in Society of Photo-Optical Instrumentation Engineers (SPIE) Conference Series, Vol. 9147, Ground-based and Airborne Instrumentation for Astronomy V, ed. S. K. Ramsay, I. S. McLean, & H. Takami, 91471G, doi: 10.1117/12.2056417

Mann, A. W., Gaidos, E., Mace, G. N., et al. 2016, ApJ, 818, 46, doi: 10.3847/0004-637X/818/1/46

Mann, A. W., Gaidos, E., Vanderburg, A., et al. 2017, AJ, 153, 64, doi: 10.1088/1361-6528/aa5276

Mann, A. W., Vanderburg, A., Rizzuto, A. C., et al. 2018, AJ, 155, 4, doi: 10.3847/1538-3881/aa9791

Mann, A. W., Johnson, M. C., Vanderburg, A., et al. 2020, AJ, 160, 179, doi: 10.3847/1538-3881/abae64

Martín, E. L., Lodieu, N., Pavlenko, Y., & Béjar, V. J. S. 2018, ApJ, 856, 40, doi: 10.3847/1538-4357/aaaeb8

Martin, W. C. 1960, J. Res. Natl. Bur. Stand. (U.S.), Sect. A, 64, 19, doi: 10.6028/jres.064A.003

Matsakos, T., Uribe, A., & Königl, A. 2015, A&A, 578, A6, doi: 10.1051/0004-6361/201425593

Mauas, P. J. D., Andretta, V., Falchi, A., et al. 2005, ApJ, 619, 604, doi: 10.1086/426428

Metcalf, A. J., Anderson, T., Bender, C. F., et al. 2019, Optica, 6, 233, doi: 10.1364/OPTICA.6.000233

Micela, G., Sciortino, S., Serio, S., et al. 1985, ApJ, 292, 172, doi: 10.1086/163143

Neff, J. E., Linsky, J. L., Landsman, W. B., & Carpenter, K. G. 1986, in ESA Special Publication, Vol. 263, New Insights in Astrophysics. Eight Years of UV Astronomy with IUE, ed. E. J. Rolfe & R. Wilson, 669

Newton, E. R., Mann, A. W., Kraus, A. L., et al. 2021, AJ, 161, 65, doi: 10.3847/1538-3881/abccc6

Ninan, J. P., Bender, C. F., Mahadevan, S., et al. 2018, in Society of Photo-Optical Instrumentation Engineers (SPIE) Conference Series, Vol. 10709, High Energy, Optical, and Infrared Detectors for Astronomy VIII, ed. A. D. Holland & J. Beletic, 107092U, doi: 10.1117/12.2312787

Ninan, J. P., Stefansson, G., Mahadevan, S., et al. 2020, ApJ, 894, 97, doi: 10.3847/1538-4357/ab8559

Nortmann, L., Pallé, E., Salz, M., et al. 2018, Science, 362, 1388, doi: 10.1126/science.aat5348

Núñez, A., Agüeros, M. A., Covey, K. R., et al. 2015, ApJ, 809, 161, doi: 10.1088/0004-637X/809/2/161

Öberg, K. I., Murray-Clay, R., & Bergin, E. A. 2011, ApJL, 743, L16, doi: 10.1088/2041-8205/743/1/L16

Obrien, George T., J., & Lambert, D. L. 1986, ApJS, 62, 899, doi: 10.1086/191160

Oklopčić, A. 2019, ApJ, 881, 133, doi: 10.3847/1538-4357/ab2f7f

Oklopčić, A., & Hirata, C. M. 2018, ApJL, 855, L11, doi: 10.3847/2041-8213/aaada9

Oliva, E., Origlia, L., Scuderi, S., et al. 2015, A&A, 581, A47, doi: 10.1051/0004-6361/201526291

Orell-Miquel, J., Murgas, F., Pallé, E., et al. 2022, A&A, 659, A55, doi: 10.1051/0004-6361/202142455

Owen, J. E., & Mohanty, S. 2016, MNRAS, 459, 4088, doi: 10.1093/mnras/stw959

Owen, J. E., & Wu, Y. 2013, ApJ, 775, 105, doi: 10.1088/0004-637X/775/2/105

—. 2017, ApJ, 847, 29, doi: 10.3847/1538-4357/aa890a

Perez, F., & Granger, B. E. 2007, Computing in Science and Engineering, 9, 21, doi: 10.1109/MCSE.2007.53

Pierrehumbert, R., & Gaidos, E. 2011, ApJL, 734, L13, doi: 10.1088/2041-8205/734/1/L13

Pizzolato, N., Maggio, A., Micela, G., Sciortino, S., & Ventura, P. 2003, A&A, 397, 147, doi: 10.1051/0004-6361:20021560

Poppenhaeger, K. 2022, MNRAS, doi: 10.1093/mnras/stac507

Preibisch, T., & Feigelson, E. D. 2005, ApJS, 160, 390, doi: 10.1086/432094

Rackham, B. V., Apai, D., & Giampapa, M. S. 2018, ApJ, 853, 122, doi: 10.3847/1538-4357/aaa08c

Reback, J., McKinney, W., Jbrockmendel, et al. 2020, pandas-dev/pandas: Pandas 1.1.1, v1.1.1, Zenodo, doi: 10.5281/zenodo.3993412

Reiners, A. 2012, Living Reviews in Solar Physics, 9, 1, doi: 10.12942/lrsp-2012-1

Reiners, A., Zechmeister, M., Caballero, J. A., et al. 2018, A&A, 612, A49, doi: 10.1051/0004-6361/201732054

Rizzuto, A. C., Vanderburg, A., Mann, A. W., et al. 2018, AJ, 156, 195, doi: 10.3847/1538-3881/aadf37

Salz, M., Czesla, S., Schneider, P. C., et al. 2018, A&A, 620, A97, doi: 10.1051/0004-6361/201833694

Sanz-Forcada, J., & Dupree, A. K. 2008, A&A, 488, 715, doi: 10.1051/0004-6361:20078501

Schneider, J., Rauer, H., Lasota, J. P., Bonazzola, S., & Chassefiere, E. 1998, in Astronomical Society of the Pacific Conference Series, Vol. 134, Brown Dwarfs and Extrasolar Planets, ed. R. Rebolo, E. L. Martin, & M. R. Zapatero Osorio, 241

Seager, S., & Sasselov, D. D. 2000, ApJ, 537, 916, doi: 10.1086/309088

Shetrone, M., Cornell, M. E., Fowler, J. R., et al. 2007, PASP, 119, 556, doi: 10.1086/519291

Shields, A. L., Ballard, S., & Johnson, J. A. 2016, PhR, 663, 1, doi: 10.1016/j.physrep.2016.10.003

Spake, J. J., Oklopčić, A., & Hillenbrand, L. A. 2021, AJ, 162, 284, doi: 10.3847/1538-3881/ac178a

Spake, J. J., Sing, D. K., Evans, T. M., et al. 2018, Nature, 557, 68, doi: 10.1038/s41586-018-0067-5

Stefansson, G., Hearty, F., Robertson, P., et al. 2016, ApJ, 833, 175, doi: 10.3847/1538-4357/833/2/175

Stefansson, G., Cañas, C., Wisniewski, J., et al. 2020, AJ, 159, 100, doi: 10.3847/1538-3881/ab5f15

Tofflemire, B. M., Rizzuto, A. C., Newton, E. R., et al. 2021, AJ, 161, 171, doi: 10.3847/1538-3881/abdf53

Tran, Q. H., Bowler, B. P., Cochran, W. D., et al. 2021, AJ, 161, 173, doi: 10.3847/1538-3881/abe041

van der Walt, S., Colbert, S. C., & Varoquaux, G. 2011, Computing in Science and Engineering, 13, 22, doi: 10.1109/MCSE.2011.37

Vanderburg, A., Mann, A. W., Rizzuto, A., et al. 2018, AJ, 156, 46, doi: 10.3847/1538-3881/aac894

Vidal-Madjar, A., Lecavelier des Etangs, A., Désert, J. M., et al. 2003, Nature, 422, 143, doi: 10.1038/nature01448

Virtanen, P., Gommers, R., Oliphant, T. E., et al. 2020, Nature Methods, 17, 261, doi: 10.1038/s41592-019-0686-2

Vissapragada, S., Stefánsson, G., Greklek-McKeon, M., et al. 2021, AJ, 162, 222, doi: 10.3847/1538-3881/ac1bb0

Wang, L., & Dai, F. 2021, ApJ, 914, 98, doi: 10.3847/1538-4357/abf1ee

Wolff, S. C., & Heasley, J. N. 1984, PASP, 96, 231, doi: 10.1086/131326

Wolfgang, A., & Lopez, E. 2015, ApJ, 806, 183, doi: 10.1088/0004-637X/806/2/183

Wright, J. T., & Eastman, J. D. 2014, PASP, 126, 838, doi: 10.1086/678541

Zarro, D. M., & Zirin, H. 1986, ApJ, 304, 365, doi: 10.1086/164170

Zhang, M., Knutson, H. A., Wang, L., Dai, F., & Barragán, O. 2022, AJ, 163, 67, doi: 10.3847/1538-3881/ac3fa7

Zirin, H. 1975, ApJL, 199, L63, doi: 10.1086/181849

—. 1976, ApJ, 208, 414, doi: 10.1086/154621